Publication Year	2021
Acceptance in OA	2025-01-14T14:33:52Z
Title	Milky Way archaeology using RR Lyrae and type II Cepheids. I. The Orphan stream in 7D using RR Lyrae stars
Authors	Prudil, Z., Hanke, M., Lemasle, B., Crestani, J., Braga, V. F., FABRIZIO, Michele, Koch-Hansen, A. J., Bono, G., Grebel, E. K., Matsunaga, N., Marengo, M., Oliveira Da Silva, Ronaldo, DALL'ORA, Massimo, Martínez-Vázquez, C. E., ALTAVILLA, Giuseppe, Lala, H., Chaboyer, B., Ferraro, I., Fiorentino, G., Gilligan, C., NONINO, Mario, Thévenin, F.
Publisher's version (DOI)	10.1051/0004-6361/202140422
Handle	http://hdl.handle.net/20.500.12386/35635
Journal	ASTRONOMY & ASTROPHYSICS
Volume	648

A&A 648, A78 (2021)
https://doi.org/10.1051/0004-6361/202140422

Astronomy & Astrophysics

Milky Way archaeology using RR Lyrae and type II Cepheids

I. The Orphan stream in 7D using RR Lyrae stars

Z. Prudil[1], M. Hanke[1], B. Lemasle[1], J. Crestani[2,3,4], V. F. Braga[3,5], M. Fabrizio[3,5], A. J. Koch-Hansen[1], G. Bono[2,3], E. K. Grebel[1], N. Matsunaga[6], M. Marengo[7], R. da Silva[3,5], M. Dall'Ora[8], C. E. Martínez-Vázquez[9], G. Altavilla[3,5], H. Lala[1], B. Chaboyer[10], I. Ferraro[3], G. Fiorentino[3], C. Gilligan[10], M. Nonino[11], and F. Thévenin[12]

[1] Astronomisches Rechen-Institut, Zentrum für Astronomie der Universität Heidelberg, Mönchhofstr. 12-14, 69120 Heidelberg, Germany
e-mail: `prudilz@ari.uni-heidelberg.de`
[2] Dipartimento di Fisica, Università di Roma Tor Vergata, via della Ricerca Scientifica 1, 00133 Roma, Italy
[3] INAF – Osservatorio Astronomico di Roma, via Frascati 33, 00078 Monte Porzio Catone, Italy
[4] Departamento de Astronomia, Universidade Federal do Rio Grande do Sul, Av. Bento Gonçalves 6500, Porto Alegre 91501-970, Brazil
[5] Space Science Data Center, via del Politecnico snc, 00133 Roma, Italy
[6] Department of Astronomy, The University of Tokyo, 7-3-1 Hongo, Bunkyo-ku, Tokyo 113-0033, Japan
[7] Department of Physics and Astronomy, Iowa State University, Ames, IA 50011, USA
[8] INAF – Osservatorio Astronomico di Capodimonte, Salita Moiariello 16, 80131 Napoli, Italy
[9] Cerro Tololo Inter-American Observatory, NSF's National Optical-Infrared Astronomy Research Laboratory, Casilla 603, La Serena, Chile
[10] Department of Physics and Astronomy, Dartmouth College, Hanover, NH 03755, USA
[11] INAF – Osservatorio Astronomico di Trieste, Via G. B. Tiepolo 11, 34143 Trieste, Italy
[12] Université de Nice Sophia-antipolis, CNRS, Observatoire de la Côte d'Azur, Laboratoire Lagrange, BP 4229, 06304 Nice, France

Received 26 January 2021 / Accepted 29 January 2021

ABSTRACT

We present a chemo-dynamical study of the Orphan stellar stream using a catalog of RR Lyrae pulsating variable stars for which photometric, astrometric, and spectroscopic data are available. Employing low-resolution spectra from the Sloan Digital Sky Survey (SDSS), we determined line-of-sight velocities for individual exposures and derived the systemic velocities of the RR Lyrae stars. In combination with the stars' spectroscopic metallicities and *Gaia* EDR3 astrometry, we investigated the northern part of the Orphan stream. In our probabilistic approach, we found 20 single mode RR Lyrae variables likely associated with the Orphan stream based on their positions, proper motions, and distances. The acquired sample permitted us to expand our search to nonvariable stars in the SDSS dataset, utilizing line-of-sight velocities determined by the SDSS. We found 54 additional nonvariable stars linked to the Orphan stream. The metallicity distribution for the identified red giant branch stars and blue horizontal branch stars is, on average, -2.13 ± 0.05 dex and -1.87 ± 0.14 dex, with dispersions of 0.23 and 0.43 dex, respectively. The metallicity distribution of the RR Lyrae variables peaks at -1.80 ± 0.06 dex and a dispersion of 0.25 dex. Using the collected stellar sample, we investigated a possible link between the ultra-faint dwarf galaxy Grus II and the Orphan stream. Based on their kinematics, we found that both the stream RR Lyrae and Grus II are on a prograde orbit with similar orbital properties, although the large uncertainties on the dynamical properties render an unambiguous claim of connection difficult. At the same time, the chemical analysis strongly weakens the connection between both. We argue that Grus II in combination with the Orphan stream would have to exhibit a strong inverse metallicity gradient, which to date has not been detected in any Local Group system.

Key words. Galaxy: halo – Galaxy: kinematics and dynamics – Galaxy: structure – stars: variables: RR Lyrae

1. Introduction

The Milky Way (MW) halo holds fossil records of its formation history where passing smaller stellar systems were tidally disrupted by the Galactic gravitational field and subsequently mixed with the insitu MW stellar populations. The relics of past mergers can be found in the form of stellar streams and overdensities (e.g., Helmi et al. 1999; Belokurov et al. 2006, 2007; Grillmair & Dionatos 2006; Grillmair 2006; Bell et al. 2008; Newberg & Carlin 2016; Shipp et al. 2018; Malhan & Ibata 2018; Helmi 2020), with their spatial and kinematical distribution carrying an imprint of the underlying MW potential and mass distribution (e.g., Johnston et al. 1999, 2005; Ibata et al. 2001; Newberg et al. 2002; Law & Majewski 2010; Koposov et al. 2010; Küpper et al. 2015; Erkal et al. 2019). The morphology of stellar streams may also provide insight into the dark matter subhalos predicted by the Λ cold dark matter (ΛCDM) cosmology (e.g., Dekel & Silk 1986; Kauffmann et al. 1993; Springel et al. 2008). In particular, dynamically cold streams can be utilized in the search for "gaps" (de Boer et al. 2020) caused by a stream encounter with a dark matter subhalo (e.g., Ibata et al. 2002; Carlberg 2012; Erkal & Belokurov 2015; Bonaca et al. 2019), and they can possibly provide a lower limit on the size of dark matter subhalos (e.g., Bode et al. 2001; Hu et al. 2000; Bullock & Boylan-Kolchin 2017). Yet, a cautious treatment of the gaps is needed since epicyclic motion and giant molecular clouds can produce such stream features as well (Amorisco et al. 2016; Ibata et al. 2020).

The advent of large photometric, spectroscopic, and astrometric surveys uncovered a wealth of stellar substructures in the MW halo (e.g., York et al. 2000; Abbott et al. 2018; Kaiser et al. 2010; Gaia Collaboration 2021; Helmi et al. 2018; Belokurov et al. 2018; Malhan & Ibata 2018). Currently, the MW halo hosts over 60 known tidally disrupted remnants of globular clusters and dwarf galaxies (e.g., Newberg & Carlin 2016; Mateu et al. 2018; Ibata et al. 2019). Among the most prominent is the Orphan stellar stream, independently discovered by Grillmair (2006) and Belokurov et al. (2007) in the Sloan Digital Sky Survey (SDSS, York et al. 2000).

The width of the Orphan stream ranges between 1−2 deg and spans across 210 deg on the sky (Newberg & Carlin 2016; Koposov et al. 2019), and it is traced out to a distance ≈60 kpc in both the southern and northern hemispheres (Koposov et al. 2019). The chemical composition of the likely stream members derived from SDSS low-resolution spectra exhibits a broad metallicity distribution with a mean at −2.1 dex and spanning from −1.5 dex up to approximately −3.0 dex (Newberg et al. 2010; Sesar et al. 2013), both for blue horizontal branch (BHB) stars and for horizontal branch pulsators (RR Lyrae stars, see below). The broad metallicity distribution (more than 1 dex) of the Orphan stream was later confirmed through low- and high-resolution spectroscopy (Casey et al. 2013, 2014), which solidified the dwarf-galaxy origin (Sales et al. 2008) on the basis of their chemical abundance patterns. Also, such a broad metallicity distribution implies a prolonged star formation history, which is expected in the dwarf-galaxy paradigm.

The dwarf nature of the Orphan stream's progenitor is further hinted at in the stream's velocity dispersion ∼10 km s^{-1} (Newberg et al. 2010). A slightly lower velocity dispersion was reported by Casey et al. (2013, 6.5 km s^{-1}), which was later corroborated by Koposov et al. (2019) and Fardal et al. (2019) placing the velocity dispersion at ≈5 km s^{-1} and ≈7 km s^{-1}, respectively, still within the boundaries expected for a tidally disrupted, dwarf-like progenitor (e.g., Gilmore et al. 2007; Koch 2009; McConnachie 2012). The orbital modeling of the Orphan stellar stream suggests a prograde orbit with an eccentricity of $e \sim 0.7$, a pericentric distance of 16.4 kpc, and an apocentric distance of 90 kpc (Newberg et al. 2010). Recently, it has been shown that the velocity vector of the Orphan stream along its track is highly perturbed by the interaction with the Large Magellanic Cloud (Erkal et al. 2019).

The name Orphan comes from the long-standing issue of the unknown progenitor. Initial searches tried to link Orphan to the Ursa Major II and Segue 1 dwarf spheroidal galaxies (Fellhauer et al. 2007; Newberg et al. 2010). Both dwarfs were later ruled out as Orphan progenitors on basis of their proper motions and distances (Koposov et al. 2019) and satellite disruption modeling (Sales et al. 2008). One candidate remained, the ultra-faint dwarf (UFD) galaxy Grus II, found in the Dark Energy Survey (DES, Drlica-Wagner et al. 2015; Abbott et al. 2018). Based on the sky position, proper motions, and distances Grus II, can be linked to the southern part of the Orphan stream (Koposov et al. 2019), although spectroscopic information such as line-of-sight velocities and chemical abundances are essential for solidifying their connection.

As a means of studying the Orphan stream, in our project we rely on pulsating variable stars of the RR Lyrae class. RR Lyrae variables are located inside the instability strip on the horizontal branch, and they are associated with old stellar populations with ages above 10 Gyr (Catelan 2009; VandenBerg et al. 2013; Savino et al. 2020). They are divided into three groups representing their pulsation mode: RRab (fundamental), RRc (first-overtone), and RRd (double-mode, pulsating simultaneously in the fundamental and first overtone mode) pulsators. Their pulsation periods are tightly connected to their luminosity (on wavelengths redder than R-band, through period-luminosity-metallicity relations, PLZ, Catelan et al. 2004; Muraveva et al. 2018; Neeley et al. 2019), and thus RR Lyrae stars serve as excellent distance indicators within the MW. In addition, the shape of their light curves reflects their chemical composition (Jurcsik & Kovacs 1996; Smolec 2005; Hajdu et al. 2018), thereby expanding their potential as tracers of the Galactic substructure and chemical composition. The aforementioned traits of RR Lyrae stars made them invaluable in studies of stellar streams in the MW halo (see, e.g., Sesar et al. 2013; Mateu et al. 2018; Hendel et al. 2018; Koposov et al. 2019; Price-Whelan et al. 2019). In our work, we build on studies by Sesar et al. (2013), Hendel et al. (2018), Fardal et al. (2019), and Koposov et al. (2019) who used RR Lyrae stars to examine the Orphan stream.

We present the first paper of the series focused on the Milky Way archaeology using old classical pulsators. This paper aims at providing line-of-sight velocities and metallicities for the members of the Orphan stream alongside a discussion of a potential Orphan progenitor. The manuscript is organized in the following manner: Section 2 outlines the dataset we built together with the cuts we imposed and the distances that were estimated. Subsequently, in Sect. 3, we describe the method we used for estimating the membership probability on basis of Bayesian inference. Section 4 illustrates the spatial and kinematical distribution of RR Lyrae variables from the assembled catalog associated with the Orphan stream. From the properties of the RR Lyrae population we were also able to recover non-pulsating stars in the SDSS catalog that are likely Orphan members. Both the method and the properties of these stars are described in Sects. 3 and 4. In Sect. 5 we discuss the possible metallicity gradient in the Orphan stream together with the orbital and chemical properties of Orphan members in context with the proposed Orphan progenitor. Final remarks are provided in Sect. 6.

2. Properties of the RR Lyrae sample

As initial sample of RR Lyrae stars, we used the catalog of pulsating variables from the early second data release of the *Gaia* mission (DR2, Clementini et al. 2019) and found matches in the early third data release of the *Gaia* source table (EDR3, Gaia Collaboration 2021) in combination with RR Lyrae stars identified in the Catalina sky survey (CSS, Drake et al. 2009) to avoid possible misclassification (Molnár et al. 2018). This sample provided us with some of the pulsation properties (pulsation periods) and astrometry (precise coordinates and proper motions; Lindegren et al. 2021) necessary for our study.

Subsequently, we cross-matched our RR Lyrae sample with the spectroscopic part of the fifteenth data release of the SDSS (Aguado et al. 2019). The SDSS provides spectra collected over two decades using two multi-object fiber-fed spectrographs, namely SDSS[1] and BOSS[2], which share comparably low-resolutions ($R \sim 2000$) and a similar wavelength range from

---

[1] Used for the two phases of the Sloan Extension for Galactic Understanding and Exploration surveys (SEGUE I and SEGUE II; Yanny et al. 2009; Eisenstein et al. 2011).

[2] Designed for the Baryon Oscillation Spectroscopic Survey (Smee et al. 2013; Dawson et al. 2013).

approximately 3600 Å–10 400 Å. Both spectrographs use optical fibers that are plugged into the plates for a given observational field (640 fibers per plate for SDSS and 1000 fibers for BOSS plates), and have blue (≈3600 Å–6000 Å) and red (≈5800 Å–10 400 Å) channels which are in the postprocessing co-added into the final data product (Stoughton et al. 2002).

SDSS targeted stellar objects mainly in the range 14–20 mag in the g-band, covering a large portion of the northern sky. Individual targets are given a `specObjID` identifier, which is generated based on the Modified Julian Date (MJD) of the observation (midpoint of the exposure), plate, and fiber ID. A fraction of our RR Lyrae stars has been observed multiple times using different fibers, plates, and in some cases by both spectrographs. Each cross-matched RR Lyrae star[3] has one `bestObjID` identifier, which serves as a reference throughout our study, and one or several `specObjID`'s. We recovered spectroscopic data for the cross-matched sample from the SDSS Science Archive Server[4]. The retrieved data products contained the co-added (merged across epochs and for both channels) spectra together with the individual exposures for both channels (blue and red) and the precise time of the observation in MJD. The method for obtaining systemic velocities (corrected for the pulsation velocity) for individual RR Lyrae variables is described in Appendix B.

We note that the SDSS provides stellar parameters (e.g., metallicities, effective temperatures, and radial velocities) that were derived by the SEGUE stellar parameter pipeline (SSPP, Lee et al. 2008a,b; Allende Prieto et al. 2008) for a large portion of our sample. These parameters were derived from the co-added spectra taken over several hours (sometimes across several days). Our targets rapidly change their radius (with radial velocity amplitudes up to 130 km s^{-1}, Liu 1991; Sesar 2012) and effective temperatures ≈1000 K (e.g., For et al. 2011; Pancino et al. 2015; Jurcsik et al. 2018) in a matter of hours. Therefore, we used the combined spectra only for a comparison to our stellar parameters that were derived from the individual spectra (usualy taken with 900 s exposures).

To secure the purity of our sample, we obtained multi-epoch photometry from the CSS for our cross-matched *Gaia* – SDSS sample[5]. The CSS observes a portion of the northern and southern sky in the effort to find and monitor near-Earth objects, and as a by-product provides a large catalog of variable objects (Drake et al. 2013a,b, 2014; Abbas et al. 2014). The CSS conducts unfiltered observations (with a subsequent calibration to V-band using Landolt standard star catalog, Landolt & Uomoto 2007; Landolt 2009) to increase the signal-to-noise ratio and detects faint objects down to ~20 mag with a single 30 s exposure (Drake et al. 2013a). The number of epochs for each object ranges from a few dozens to almost a thousand with an average uncertainty of 0.1 mag. We verified the periodicity of the objects in our initial sample and obtained their ephemerides and pulsation properties. The details of this analysis can be found in Appendix A.

2.1. The astrometric sample

For the purpose of using our catalog to study stellar streams, a precise astrometric solution including distances and a thorough treatment of their uncertainties is essential. In order to carefully assess the proper motions for individual variables we followed Hanke et al. (2020) and Prudil et al. (2020), and utilized the values provided by *Gaia*'s EDR3 for proper motions in right ascension and declination (μ_{α^*}, μ_{δ}), their uncertainties ($\sigma_{\mu_{\alpha}^{*}}$, $\sigma_{\mu_{\delta}}$), covariances ($\rho_{\mu_{\alpha}^{*},\, \mu_{\delta}}$), and re-normalized unit weight error (RUWE[6]).

In the first step, we scaled the covariance matrix, Σ, by the RUWE^2 factor, and diagonalized the resulting scaled covariance matrix by its eigenvectors (resulting in the transformed Σ*). Using the eigenvectors of the covariance matrix, we transformed the vector composed of the stars' proper motions, **V**, and required at least 3σ confidence in the scaled sum of the transformed proper motions:

$$\sqrt{\sum \mathbf{V}^2/\mathrm{tr}(\mathbf{\Sigma}^*)} > 3.0. \tag{1}$$

This reduced our sample size from 4247 to 3970 RR Lyrae with at least 3σ significant proper motions.

2.2. Distance estimates

The connection of the RR Lyrae stars' pulsation periods, metallicities, and luminosities permits us to estimate a distance to a given RR Lyrae star with an uncertainty on the order of three and ten percent for infrared and optical data, respectively (Neeley et al. 2017). The literature provides many PLZ relations both from the theoretical (e.g., Catelan et al. 2004; Marconi et al. 2015, 2018), and observational studies (e.g., Muraveva et al. 2018; Neeley et al. 2019). The importance of metallicity in the PLZ relations and distance calculation is small as we move from the optical to the infrared wavelengths, it does not completely disappear, and the absence of a metallicity estimate for an individual star introduces an additional source of uncertainty on its distance estimate.

Our data set is composed of unfiltered CSS photometry for which we estimated the mean magnitude based on a Fourier decomposition (see Appendix A). Unfortunately, absolute magnitudes of RR Lyrae stars in the V-band are strongly dependent on metallicity, and not on pulsation period (see Catelan et al. 2004; Marconi et al. 2018; Muraveva et al. 2018).

To overcome this drawback, one needs to move from the visual wavelengths more toward the near-infrared or rely on the period-Wesenheit-metallicity (PWZ) relations, which provide a solid diagnostic for individual RR Lyrae distances due to its low metallicity dependence. For this reason, we decided to cross-match our RR Lyrae sample with the PanSTARRS-1[7] (PS1, Chambers et al. 2016) catalog of RR Lyrae stars (Sesar et al. 2017), and utilized their flux-averaged i-band magnitudes. The PLZ in the PS1 i-passband is strongly dependent on the pulsation period and only marginally on metallicity (see Table 1 in Sesar et al. 2017). In order to estimate distances to the first-overtone pulsators we needed to transform their pulsation periods (P_{1O} – pulsation period of the first overtone mode) into the corresponding fundamental periods (P_{F} – pulsation period of the fundamental mode) using the relation from Iben & Huchra (1971) and Braga et al. (2016):

$$\log P_{\mathrm{F}} = \log P_{\mathrm{1O}} + 0.127. \tag{2}$$

We note that there are several other approaches on how to transform the pulsation periods of RRc type stars (e.g.,

---

[3] Based on equatorial coordinates with a radius of 10 arcsec.

[4] https://dr15.sdss.org/sas/dr15/

[5] Using the web interface: http://nesssi.cacr.caltech.edu/cgi-bin/getmulticonedb_release2.cgi

[6] The RUWE serves as an informative statistic on the quality of the astrometric five-parameter solution. We refer the interested reader to the technical note http://www.rssd.esa.int/doc_fetch.php?id=3757412 for more details.

[7] Panoramic Survey Telescope and Rapid Response System.

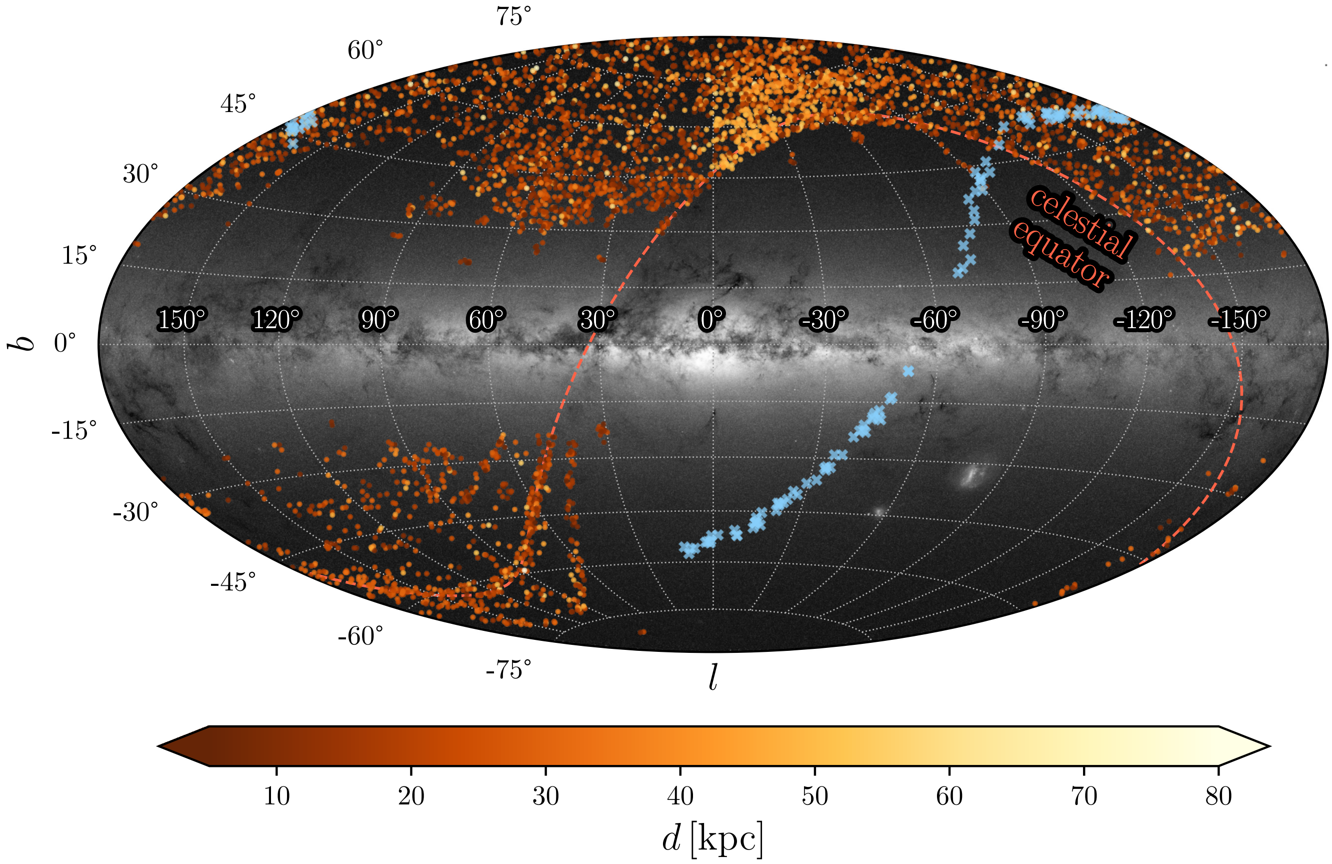

Fig. 1. Spatial distribution of RR Lyrae stars (color-coded based on their distance) in Galactic coordinates. The light blue crosses denote the RR Lyrae stars associated with the Orphan stream by Koposov et al. (2019). *Gaia*'s all-sky star density map is underlaid in the background as illustration. Image credit: *Gaia* Data Processing and Analysis Consortium (DPAC); A. Moitinho/A. F. Silva/M. Barros/C. Barata, University of Lisbon, Portugal; H. Savietto, Fork Research, Portugal.

Di Criscienzo et al. 2004; Coppola et al. 2015), but their effect on the resulting absolute magnitude and subsequently distance is only marginal, and is complety covered by the total error budget of the absolute magnitude of a given star. To obtain metallicities for the i-band PLZ relation, we used samples analyzed by Fabrizio et al. (2019) and Crestani et al. (2021) which largely (>90%) overlap our sample. To account for the missing metallicity in the remaining ten percent of the stars in our sample, we assumed a single value using the average and standard deviation by Crestani et al. (2021) ($[\mathrm{Fe/H}] = -1.55 \pm 0.51$ dex) for halo RR Lyrae stars. To account for the reddening of the sample stars we utilized the extinction maps from Schlafly & Finkbeiner (2011).

To calculate distances, d, and their uncertainties, σ_d, we ran a Monte Carlo error analysis where we assumed a Gaussian distribution for the uncertainties on apparent magnitudes of 0.1 mag error on each i-band magnitude. We also varied the coefficients of the PLZ relation (for the i-passband as listed in Table 1 in Sesar et al. 2017), within their errors, together with our assumed metallicities, reddening coefficients, and their associated uncertainties. The resulting distances range from 4 to 100 kpc with the error budget varying from five to six percent. We note that our uncertainties are larger than generally reported for the PS1 survey of RR Lyrae stars (e.g., Sesar et al. 2017, reported uncertainties around three percent). This is mainly due to our assumed error on the apparent magnitude, which we believe better represents the sparsity of PS1 observations. In Fig. 1 we depict the distribution of our selected RR Lyrae variables with estimated distances. We show only the stars whose proper motions satisfy Eq. (1).

As a validation check of our derived distances, we cross-matched our sample with the *Spitzer* Merger History and Shape of the Galactic Halo (SMASH) sample of RR Lyrae stars for the Orphan stream assembled by Hendel et al. (2018) and found 17 variables in common. We detected a small offset of approximately 0.7 kpc between both sets of distances, a value roughly two to four times smaller than the individual uncertainties assigned to our distances and therefore negligible.

3. Membership method

To assess a star's possible association with a given stellar stream, we employed a probabilistic approach similar to the one used for classical Cepheids in open clusters by Anderson et al. (2013), and a study of MW globular cluster escapees in the halo (Hanke et al. 2020). In our analysis we establish membership probabilities based on the Bayesian framework that states that the posterior probability $p(A|B)$ of a model for the stream, A, and the data, B, is:

$$p(A|B) = \frac{p(B|A) \times p(A)}{p(B)} \propto p(B|A) \times p(A), \tag{3}$$

which is a product of the likelihood function $p(B|A)$, our prior belief in an association, $p(A)$, and a normalizing constant, $p(B)$, representing the probability of observing the data

(Bayes & Price 1763). Our analysis focused on connecting our sample of RR Lyrae variables with the Orphan stellar stream which is sufficiently defined in equatorial coordinates α, δ, proper motions: μ_{α^*}, μ_δ, and distances d.

Thus, we selected the prior to be a uniform probability distribution (with upper and lower boundaries) on the sky position α:

$$p(A) = 1 \texttt{ if } \mathrm{Min}\left(\left|\alpha^{\mathrm{stream}} - \alpha^{\mathrm{RR}\star}\right|\right) < 5\,\mathrm{deg} \texttt{ else } 0. \tag{4}$$

For a simple description of stellar streams in a multi-parameter space, we used the Gaussian process (GP) regressor implemented in the `scikit-learn` library (Pedregosa et al. 2011). The GPs are a Bayesian nonparametric approach to regression, and they are a useful tool for nonlinear regression and classification. In the GP regressor we predict a continuous variable by specifying a suitable covariance function (kernel). In our case we selected the following set of kernels and their hyperparameters[8]:

```
kernel = (ConstantKernel() +
          WhiteKernel(noise_level=2) +
          Matern(length_scale=2, nu=3/2))
      × 0.025² · DotProduct(sigma_0=1.0,
                 sigma_0_bounds=(0.1, 10.0)).
```

The optimization of the kernels' hyperparameters is performed internally by the optimizer based on the maximization of the log marginal likelihood instead of the computationally expensive cross-validation. We refer the interested reader to Rasmussen & Williams (2005) for a comprehensive and detailed description of GPs.

Using GPs, we fitted the parameters $\delta, \mu_{\alpha^*}, \mu_\delta$, and d as a function of α for the bona fide members of the Orphan stellar stream (Koposov et al. 2019), and obtained a GP regression model for the aforementioned parameters. The individual models, when provided with α, predict values and covariances for a given parameter.

In order to estimate the conditional likelihood $p(B|A)$, we followed the example by Anderson et al. (2013) and Hanke et al. (2020), and utilized the Mahalobis distance[9] (Mahalanobis 1936):

$$D_M^2 = \left(\mathbf{x}^{\mathrm{RR}\star} - \mathbf{x}^{\mathrm{stream}}\right)^{\mathrm{T}} \mathbf{\Sigma}^{-1} \left(\mathbf{x}^{\mathrm{RR}\star} - \mathbf{x}^{\mathrm{stream}}\right), \tag{5}$$

where $\mathbf{x}^{\mathrm{RR}\star}$ is a four-component vector composed of equatorial coordinates, proper motions, and distances ($\mathbf{x}^{\mathrm{RR}\star} = \{\delta, \mu_{\alpha^*}, \mu_\delta, d\}$) for a given α-coordinate. For obtaining a star's stream vector $\mathbf{x}^{\mathrm{stream}}$ we used as an input to the GP regression the star's equatorial α coordinate. The Gaussian regression models in turn yield a prediction for $\mathbf{x}^{\mathrm{stream}}$ and their variance for the streams' covariance matices. The visual depiction of our analysis can be found in Fig. 2. $\mathbf{\Sigma}^{-1}$ represents the inverse sum of covariance matrices between an RR Lyrae variable and a given stellar stream scaled by the squared RUWE. The covariance matrix for RR Lyrae stars in our sample was constructed using the variances and correlation coefficients from *Gaia* EDR3. Since our distances came from an independent source, we set their correlations with other parameters to zero. The stream covariance matrix is built using the prediction on the individual parameter

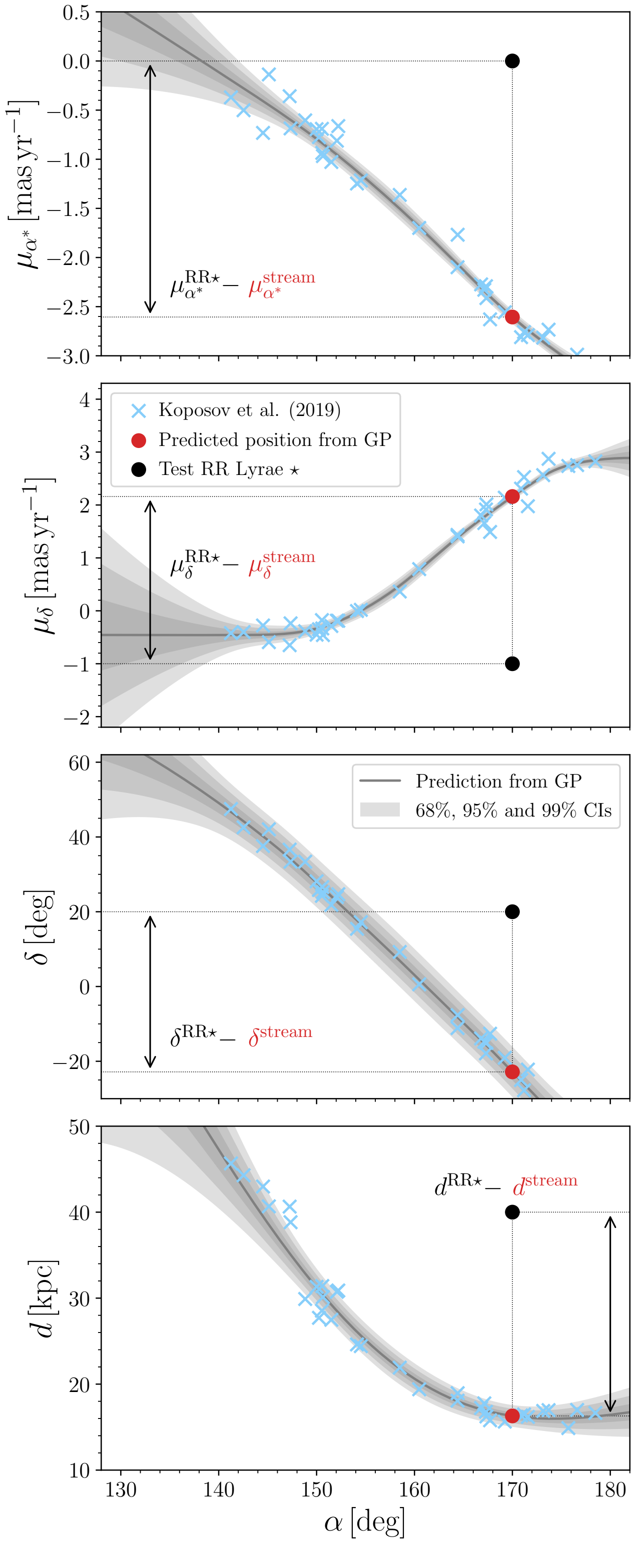

Fig. 2. Visual example of the membership analysis for the Orphan stellar stream using data from Koposov et al. (2019) (blue crosses), with an artificially placed star (black dot), and its stream counterpart (red dot) at the same α and predicted values of $\delta, \mu_{\alpha^*}, \mu_\delta$, and d. Black solid lines and gray shaded regions denote the GP regression and its confidence intervals (CIs, $\pm1, 2, 3\sigma$), respectively.

from the GP regressor and only contains diagonal entries. To ensure that our stream quantities are independent of the variable

---

[8] We note that for the individual regressions we varied the individual covariance functions. The GP models for individual parameters will be provided at `https://github.com/ZdenekPrudil/Orphan2020`

[9] Which in practice is a generalized Euclidean distance (with the identity covariance matrix), and is often used for the identification of outliers (Kim 2000).

sample (no covariance between $\mathbf{x}^{\mathrm{RR}\star}$ and $\mathbf{x}^{\mathrm{stream}}$) we removed cross-matched RR Lyrae stars from the parent population of the stream sample for the GP regression of the stream distributions.

Because of the assumption of a multivariate-normal error distribution the resulting D^2_M is chi-squared distributed, in our case with four degrees of freedom (coordinate, proper motions, and distance). The likelihood function $p(B|A)$ can then be expressed as a p-value (p_{val}) of the D^2_M;

$$p(B|A) = 1 - p_{\mathrm{val}}(D^2_M). \tag{6}$$

The p-value is a probability metric for evaluating the null hypothesis, which in our case is a hypothesis test whether a star is or is not associated with a given stellar stream. A high p-value in Eq. (6) highlights stars that we considered as outliers from the stream. Thus, our probability calculation mainly tags the stream's outliers (nonmembers). Conversely, if a high number of explored dimensions is provided, with strong constraints on the significance of individual parameters, then the probability of a star's membership in a given stream increases. We note that just as in any general case, the null hypothesis cannot be proven but only excluded. Thus, we treat the identified members as likely associations.

With the goal to distinguish between outliers and possible members, we selected for $p(A|B)$ a critical threshold of 0.05. Thus the RR Lyrae stars in our sample with a higher $p(A|B)$ will be treated as tentative stream members.

4. RR Lyrae and non-pulsating stars in the Orphan stream

4.1. RR Lyrae stars in the Orphan stream

Since its discovery (Grillmair 2006; Belokurov et al. 2007), the Orphan stream has been targeted by various studies that provided several lists of possible candidates representing a variety of stellar types (e.g., F-turnoff stars, BHB stars, RR Lyrae stars, and K-giants, Newberg et al. 2010; Sesar et al. 2013; Koposov et al. 2019; Casey et al. 2013). The sample from Newberg et al. (2010) is based on the SDSS photometric and spectroscopic products, providing important spatial, dynamical, and chemical information about the Orphan stream, especially the metallicities of the BHB stars ([Fe/H] = −2.1 dex), and their spread hint toward the progenitor of the Orphan stream being a dwarf galaxy.

The work by Sesar et al. (2013) confirmed the mean metallicity of the Orphan stream and its large spread found by Newberg et al. (2010), and provided precise distances to individual RR Lyrae stars effectively tracing the Orphan stream out to 55 kpc. The first detailed chemical abundance study of the Orphan stream by Casey et al. (2013) provided stream candidates based on their spatial, kinematic, and chemical properties. The associated K-giants exhibit a slightly more metal-rich composition ([Fe/H] = −1.63 dex) than the BHB stars. We note that in the high-resolution spectroscopic study of Casey et al. (2014), three high-probable candidates that can be kinematically and astrometrically associated with the Orphan stream exhibit a slightly lower average metallicity [Fe/H] = −2.01 dex.

We use the latest sample of possible stream members from the work by Koposov et al. (2019 and from here on we refer to it as the K19 reference sample). The K19 sample includes *Gaia* EDR3 and variable stars identification from Clementini et al. (2019). It consists of 109 RR Lyrae stars (106 fulfilling the condition in Eq. (1)) associated with the Orphan stream based on their spatial and kinematical properties. The Orphan reference sample spans both Galactic hemispheres, with a total coverage of about 210 degrees, and distances ranging from ≈10 kpc to 60 kpc.

Our dataset relies on *Gaia* EDR3 astrometric products and mainly on the *Gaia* identification of RR Lyrae stars (Clementini et al. 2019) verified using the CSS and PS1 surveys, and covers primarily the northern Galactic hemisphere due to the SDSS footprint (see Fig. 1). Our dataset offers a re-evaluated RR Lyrae classification, improved distance estimates, metallicities, and systemic velocities for individual RR Lyrae stars. The RR Lyrae stars from the reference sample only served as an input for our membership analysis described in the previous section. From the K19 sample, 20 RR Lyrae stars overlap with our dataset. The K19 sample does not contain uncertainties on individual distance estimates, which are based on visual magnitudes of individual RR Lyrae variables, thus we assumed a general uncertainty of 10% on the distance estimate for the Gaussian process regression.

In Fig. 3, we show the results of our analysis for our sample of RR Lyrae located in the vicinity of the K19 dataset. In our investigation, we identified 20 RR Lyrae variables (13 RRab and 7 RRc-type pulsators) to be associated with the Orphan stream based on their equatorial coordinates, proper motions, and distances. From these stream associates, we recover 12 variables already present in the K19 sample. The remaining eight RR Lyrae pulsators consist of three variables that were identified as members of the Orphan stream by Sesar et al. (2013) and Hendel et al. (2018), while five are new discoveries. The likelihoods of stars not included in the K19 sample range from $p(A|B) = 0.05$ (by construction owing to the adopted lower threshold) up to almost $p(A|B) = 0.8$, with only four below $p(A|B) < 0.2$. Similar to the K19 sample, we trace the Orphan stream from approximately 25 kpc to 47 kpc in distance across 32 deg on the sky. The proper motion ranges are $\mu_{\alpha^*} \approx (-1.13; -0.03)$ mas yr^{-1} and $\mu_\delta \approx (-0.75; 0.07)$ mas yr^{-1} and follow by construction the ranges of the K19 RR Lyrae stars. Based on the likely stream members, the projected width of Orphan stream varies around 1−2 deg, which is similar to the findings of Grillmair (2006) and Belokurov et al. (2007). We also report a higher average metallicity for the Orphan RR Lyrae stars of [Fe/H] = −1.80(6) dex with a dispersion of 0.25 dex. This is significantly more metal-rich than previously reported by Sesar et al. (2013, average metallicity equal to −2.1 dex). This point will be discussed in Sect. 4.2. In Fig. 3 we notice that one of the apparently associated RR Lyrae variables does not fit the general systemic velocity trend. Thus, we consider it as a nonmember and remove it in the further analysis, whilst marking it with an asterisk in Table D.1. The remaining 19 RR Lyrae stars were used to assess our systemic velocities with respect to the `RV_ADOP` determined by the SSPP pipeline. Expectedly, we found a lower dispersion in our systemic velocities in comparsion to dispersion in `RV_ADOP`, 11.0 km s^{-1}and 19.5 km s^{-1}, respectively.

Using the calculated distances and estimated systemic velocities, we specifically looked for RR Lyrae stars beyond 50 kpc (the estimated apogalacticon of 90 kpc by Newberg et al. 2010), and we found no RR Lyrae stars in our sample that could be considered as a continuation of the Orphan stream. As an additional corroboration of our Orphan RR Lyrae candidates, we looked at their distribution in the period-amplitude plane and searched for high-amplitude short-period RR Lyrae variables (HASP, Fiorentino et al. 2015). The HASP RR Lyrae stars are characterized by short pulsation periods ($P < 0.48$ day) and high amplitudes (in V-band above 0.75 mag). They often occur

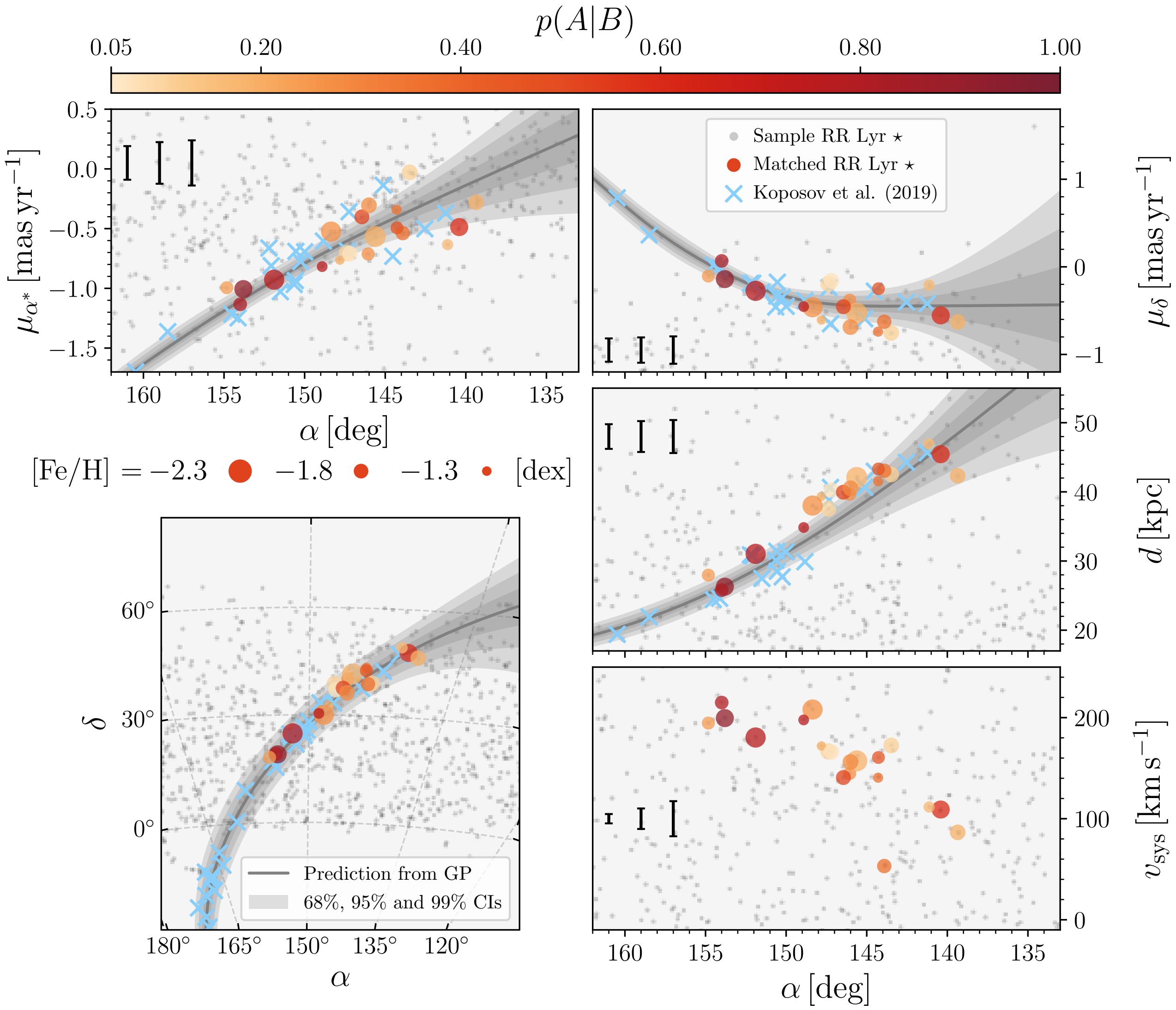

Fig. 3. Four-parameter association with the Orphan stream defined by the sample of RR Lyrae stars from Koposov et al. (2019, denoted by light blue crosses) based on the spatial and astrometric properties of the studied sample. The RR Lyrae stars associated with the Orphan stream (with a lower significance threshold set at 0.05) are color-coded based on the conditional probability $p(A|B)$. Gray dots represent rejected RR Lyrae stars from our sample. Black lines and gray regions denote the GP fit to the reference sample and confidence intervals of a given interpolation, respectively. The metallicity of each star associated with the Orphan stream is depicted by varying its point size. The error bars in the left corners represent the 15.9, 50, and 84.1 percentiles of individual parameter uncertainties for the RR Lyrae variables linked with the Orphan stream.

in systems with high metallicity (higher than −1.5 dex, such as the Galactic bulge, metal-rich globular clusters, and partially also in the Galactic halo, Fiorentino et al. 2015). Based on Orphan's low metallicity we would not expect HASPs to be found in the Orphan stellar stream and we note that indeed none of our Orphan associated RR Lyrae stars belong to the HASP group. Although one HASP RR Lyrae star has been identified in the southern portion of the Orphan stream by Martínez-Vázquez et al. (2019) which is probably caused by the large dispersion in the metallicity distribution of Orphan RR Lyrae stars that covers regions with [Fe/H] > −1.5 dex and permits such possibility.

4.2. Nonvariable stars in Orphan

Building upon the approach for RR Lyrae stars, we performed a similar analysis with the remaining stellar sample of the SDSS. To this extent, we searched for objects analyzed by the SSPP pipeline, restricting the sample to those objects with determined $T_{\rm eff}$. Utilizing SSPP products, we obtained their atmospheric parameters ($T_{\rm eff}$, $\log g$, [Fe/H]) together with their heliocentric line-of-sight velocities. The nonvariable sample, as we refer to it, was subsequently cross-matched using equatorial coordinates with the *Gaia* EDR3 catalog to acquire their proper motions and photometric properties (G, $G_{\rm BP}$, and $G_{\rm RP}$ magnitudes). Regarding the proper motion significance, we required the same significance as in the case of the RR Lyrae sample to remove possible outliers.

For our nonvariable sample, we proceeded with our method outlined in Sect. 3 (using our identified sample of Orphan RR Lyrae stars as the parent population) with two differences. Firstly, instead of using spectrophotometric distances, which can be prone to many systematics, we substituted the distance in the $\mathbf{x}^\star$ vector with the systemic velocity $\left(\mathbf{x}^\star = \left\{\delta, \mu_{\alpha^*}, \mu_\delta, v_{\rm sys}\right\}\right)$, thus slightly favoring the kinematical over the spatial association. Secondly, we only looked for tentative members close to the stream itself, thus narrowing our uniform flat prior from five degrees to one degree. As an additional criterion, we adopted cuts on metallicities and $\log g$ to select stars above the main sequence and thus remove the majority of the contributions from the Galactic disk:

$$[\mathrm{Fe/H}] < -1.0\,\mathrm{dex} \quad \cap \quad \log g < 4.0\,\mathrm{dex}. \tag{7}$$

Following this approach, we recovered 54 nonvariable stars likely associated with the Orphan stream as traced by our sample of RR Lyrae variables (listed in Table D.2). We also recovered four stars that were previously identified as RR Lyrae stars in the *Gaia* DR2 and PS1 surveys. Using CSS photometry, we were able to classify three of them as double-mode RR Lyrae pulsators. The one remaining variable has an uncertain classification. All four stars did not enter our initial analysis of single-mode RR Lyrae stars and are denoted with an asterisk in Table D.2. The distributions of astrometric and kinematical parameters of the associated nonvariables are depicted in Fig. C.1.

Utilizing the spectroscopic products (surface gravities and effective temperatures) determined by the SSPP pipeline and the dereddened photometry from *Gaia* EDR3, we constructed the Kiel diagram ($\log g$ vs. T_{eff}) and the color-magnitude diagram for stable stars associated with the Orphan stream (see Fig. 4). To deredden *Gaia* apparent magnitudes, we used the extinction coefficients from Casagrande & VandenBerg (2018, see their Table 2) in combination with the dust maps derived by Schlafly & Finkbeiner (2011). The G magnitudes of each stable star were corrected by the distance modulus estimated from the Gaussian process regression of our RR Lyrae sample given its right ascension.

In the top panel of Fig. 4 we clearly identify the red giant branch (RGB, defined as $T_{\mathrm{eff}} < 5500\,\mathrm{K}$ and $\log g < 3\,\mathrm{dex}$, seen in Fig. 4) with several stars possessing a high membership probability ($p(A|B) > 0.5$). In addition, also BHB stars between 8000 and 9000 K, and $\log g$ ranging from 3.0 to 3.5 dex were observed. We notice a discrepancy between the upper and lower panels, where for the upper panel (built with the SDSS spectroscopic products) an isochrone of metallicity −2.0 dex provides a good fit, in contrast to *Gaia* data where an isochrone of higher metallicity (−1.5 dex) is necessary. We believe that this inconsistency is rooted in the stellar parameters derived by the SDSS: Figure A2 in Smolinski et al. (2011) shows trends between stellar parameters T_{eff}, $\log g$, and [Fe/H] derived by the SDSS and those from high-resolution studies. Similar trends in stellar parameters of the SDSS survey were also independently reported by Hanke et al. (2018) and Hanke et al. (2020, based on monometallic globular clusters).

5. Discussion

The full 7D[10] chemo-dynamical distribution of RR Lyrae stars likely associated with the Orphan stream permits us to examine their orbital parameters with respect to an assumed static MW potential. Jointly with chemical information in the form of [Fe/H] for nonvariable stars associated with the Orphan stream (see Sect. 4.2) we can search for its possible progenitor. We focus on comparing with the work by K19, who provided a detailed examination of the properties of a possible Orphan progenitor regarding the stream RR Lyrae population. K19 also discussed likely progenitors among several globular clusters and dwarf galaxies based on the spatial (α, δ, and distances), and proper motion spaces.

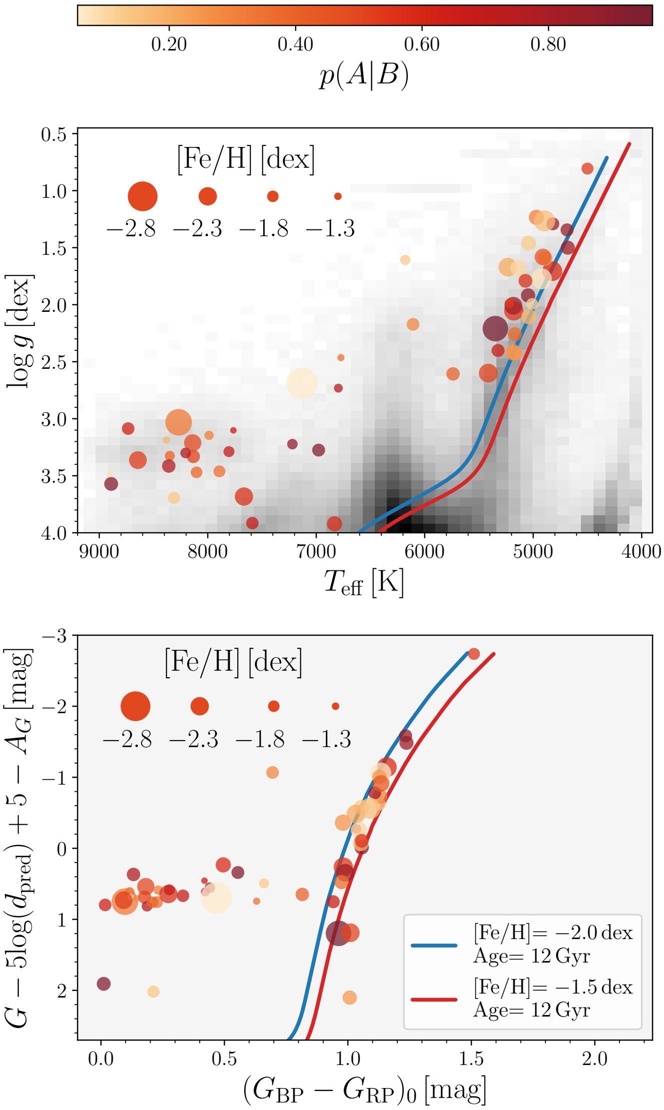

Fig. 4. Kiel diagram (*top panel*, using quantities from the SSPP pipeline), and the color-magnitude diagram (*bottom panel*) for stars likely associated with the Orphan stellar stream color-coded based on the probability and with varying point size denoting the metallicity. The blue and red lines represent isochrones from the MESA Isochrones and Stellar Tracks (MIST, Dotter 2016; Choi et al. 2016; Paxton et al. 2011, 2013, 2015) database for two different metallicities. The gray contours in the top panel represent the entire star matched sample of SDSS-*Gaia*.

5.1. On a possible metallicity gradient in Orphan

The metallicity of RGB and BHB stars centers at −2.13 ± 0.05 dex, and −1.87 ± 0.14 dex, with dispersions of 0.23 and 0.43, respectively. The average values are in good agreement with previous studies by Newberg et al. (2010) and Sesar et al. (2013), who find an average metallicity of −2.1 dex among RR Lyrae stars associated with the Orphan stream. Sesar et al. (2013) also reported a metallicity gradient in their sample of RR Lyrae stars. We explored this possibility by first cleaning the sample based on the *Gaia* astrometry, following the same steps as in the case of our RR Lyrae sample. From a

---

[10] Equatorial coordinates, distances, proper motions, line-of-sight velocities, and metallicities.

total of 50 RR Lyrae stars in the Sesar et al. (2013) catalog we recovered 20 likely members of the Orphan stream. Following Sesar et al. (2013) we calculated the Kendall's τ coefficient[11] (Kendall 1938) for the stream longitude, ϕ_1 (calculated through the coordinates tranformation matrix from K19), with respect to the metallicity for these 20 single mode RR Lyrae stars that are likely Orphan members, and we obtained $\tau^{\rm [Fe/H]}_{\phi_1} = -0.41 \pm 0.11$. This is very similar to the value reported by Sesar et al. (2013) and also significant[12].

We explored the existence of a metallicity gradient in the Orphan stream using our nonvariable and RR Lyrae sample[13]. The depiction of the metallicity versus ϕ_1 can be found in Fig. 5. In both of our samples (nonvariable and RR Lyrae sample) we do not detect any significant correlation between the sky position ϕ_1 and metallicity. A similar outcome holds even when we include only stars with a high probability $p(A|B) > 0.5$ for both of our samples. One of the possible reasons for this discrepancy lies in the different metallicity calibrations between our study and Sesar et al. (2013). In our case, we rely on the new calibration of the ΔS method using metallicities determined from high-resolution spectra (Crestani et al. 2021), while Sesar et al. (2013) relied on the calibration of Layden (1994) which is slightly offset compared to metallicities obtained from high-resolution spectra (see, e.g., For et al. 2011; Chadid et al. 2017). Another reason could lie in the metallicity scale, where Sesar et al. (2013) values lie on the Zinn & West (1984) scale[14], while our metallicities are on a different metallicity scale (Chadid et al. 2017; Sneden et al. 2017; Crestani et al. 2021). This could shift the metallicities of Sesar et al. (2013) toward the metal-rich end by up to 0.2 dex (For et al. 2011). To conclude, using our dataset we were unable to confirm the existence of a metallicity gradient in the Orphan stellar stream.

5.2. Grus II as a possible progenitor

In the work by K19, the previously considered candidates for the Orphan progenitors, Segue 1 and UMa II (Fellhauer et al. 2007; Newberg et al. 2010), were excluded based on their distance and proper motions. One viable candidate for the progenitor of the Orphan stream remained, Grus II, a UFD (found in the DES by Drlica-Wagner et al. 2015). Grus II matches with the Orphan stellar stream in the coordinates and proper motion space. Recently, line-of-sight velocities and chemical abundances became available for several stars associated with Grus II UFD (Simon et al. 2020; Hansen et al. 2020). The line-of-sight velocities center on average at $-106.7 \pm 0.2\,\mathrm{km\,s^{-1}}$ for three RGB stars analyzed by Hansen et al. (2020), and at $-110.7 \pm 0.5\,\mathrm{km\,s^{-1}}$ for identified members by Simon et al. (2020). Combining the distance and sky position of Grus II (Martínez-Vázquez et al. 2019), together with the proper motions (McConnachie & Venn 2020) and line-of-sight velocities (Simon et al. 2020) allowed us to calculate the orbital properties of Grus II, and to compare them with the orbital properties of our RR Lyrae sample associated with the Orphan stellar stream.

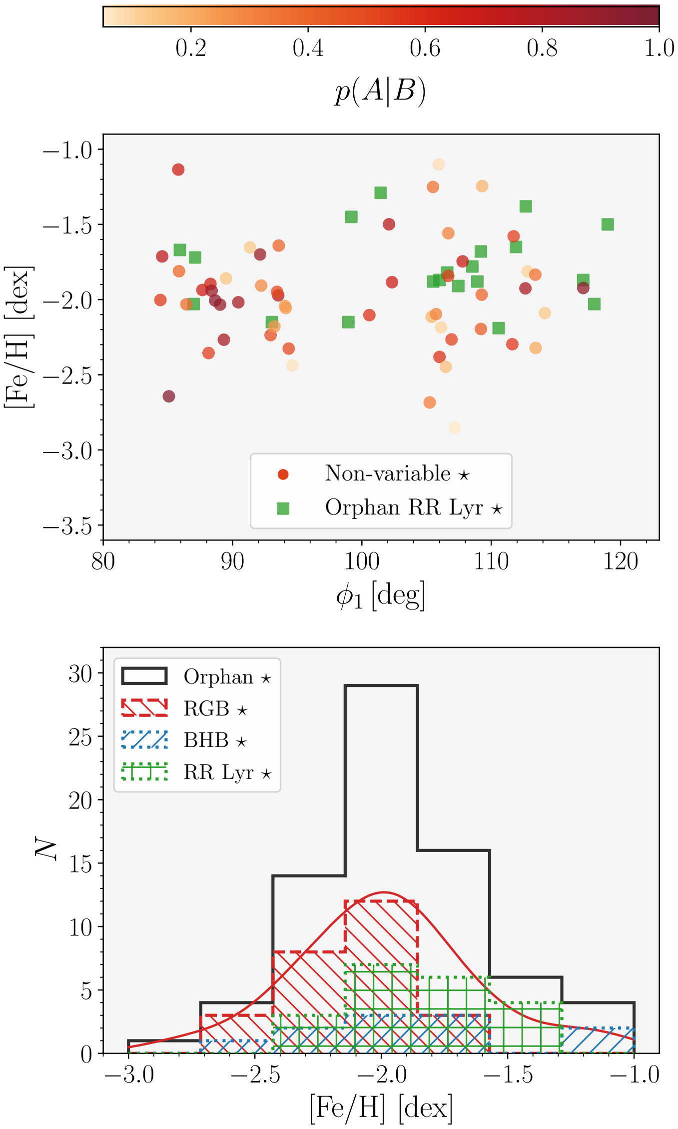

Fig. 5. Stream coordinates, ϕ_1, versus [Fe/H] (*top panel*), and metallicity distribution function (*bottom panel*) for likely variable and nonvariable Orphan stream members. The color-coding of each nonvariable star represents the probability of association to the Orphan stream $p(A|B)$, and the green squares represent RR Lyrae stars associated with the Orphan stream in our study. The histogram in the *lower panel* represents the metallicity distribution of the entire sample (black line) the RGB stars (red dashed line), BHB stars (blue dotted line), and RR Lyrae stars (green lines). The red solid line represents the kernel density estimate of the metallicity distribution of the RGB stars.

5.2.1. Dynamical association

For the purpose of examining the kinematical distribution of the identified Orphan stream members and Grus II, we utilized the `galpy v1.6`[15] package for Galactic dynamics (Binney 2012; Bovy & Rix 2013; Bovy 2015), and estimated for the entire RR Lyrae sample and Grus II the following quantities: orbital parameters (eccentricity e, excursion from the Galactic plane

---

[11] The Kendall's correlation coefficient, τ, is a nonparametric correlation test, thus independent of any assumptions on the distribution of the tested samples.

[12] We note that we calculated the uncertainty on $\tau^{\rm [Fe/H]}_{\phi_1}$ through a Monte Carlo error simulation where we assumed a Gaussian distribution for errors on the metallicity ($\sigma_{\rm [Fe/H]} = 0.2$ dex).

[13] We verified, with a sample of 3000 RRL stars, that both the new high-resolution ΔS scale and that of the SSPP pipeline metallicities agree within −0.01 dex with a dispersion of 0.28 dex without any significant trend.

[14] It is worth mentioning that the Zinn & West (1984) scale exhibits mild nonlinearity in comparison with the high-resolution studies of the MW globular clusters (see Fig. 9 in Carretta et al. 2009).

[15] Available at `http://github.com/jobovy/galpy`

$z_{\max}$, and peri- and apocenters, $r_{\rm per}$ and $r_{\rm apo}$), orbital energy E, actions $J_{\rm R}$, $J_{\rm z}$, and angular momenta $L_{\rm z}$ (J_{ϕ}) with their respective uncertainties and correlations.

In our setup, we implemented an MW potential consisting of a Miyamoto-Nagai disk ($M_{\rm disk} = 6.8 \times 10^{10}\,M_{\odot}$, $a = 3.0$ kpc, $b = 0.28$ kpc, Miyamoto & Nagai 1975)[16], a Hernquist bulge (Hernquist 1990, $M_{\rm bulge} = 6.0 \times 10^{9}\,M_{\odot}$, $a = 0.5$ kpc); and a Navarro-Frenk-White spherical halo (Navarro et al. 1997, $M_{\rm halo} = 5.4 \times 10^{11}\,M_{\odot}$, $r_{\rm s} = 16$ kpc).

As a Galactocentric reference frame, we adopted the left-hand annotation with the following values for the Solar position and motion: The distance to the Galactic center is set to $R_0 = 8.178$ kpc (Gravity Collaboration 2019), the Solar system is placed above the Galactic plane at $z_{\odot} = 20.8$ pc (Bennett & Bovy 2019). The Solar motion with respect to the local standard of rest is $(U_{\odot}, \upsilon_{\odot}, W_{\odot}) = (-11.1, 247.24, 7.25)\,{\rm km\,s^{-1}}$ (Schönrich et al. 2010; Schönrich 2012), where $V_{\odot} = \upsilon_{\odot} - V_{\rm c} = 12.24\,{\rm km\,s^{-1}}$. For each star we performed a Monte Carlo simulation taking into account the full covariance between the sky positions α, δ, and proper motions μ_{α^*}, μ_{δ}, in combination with errors in systemic velocities and distances. The estimated values were taken as an average of the generated distributions with the standard deviation representing the uncertainties on the given properties. In addition, to robustly assess the distributions of the orbital parameters, we also recovered the correlations between the individual orbital properties. Here we note that E and actions often do not follow the multivariate normal distribution, as shown, for example, in Fig. 6 in Hanke et al. (2020), and here in the bottom panel of Fig. 6. Thus, our assumption based on averages, standard deviations, and correlations here serves only to guide the eye and give an intuition on the uncertainties of estimated parameters.

The median pericentric distances of RR Lyrae stars associated with the Orphan stellar stream peak at 22 kpc. They reach on their orbit a median apocenter equal to 89 kpc, and their average eccentricity varies around 0.61. These values are similar to the orbital properties estimated by Newberg et al. (2010), who estimated eccentricities of Orphan stream stars to be 0.7 with apocentric and pericentric distances equal to ≈90 kpc, and 16 kpc, respectively. In the case of Grus II, the UFD reaches apocentric and pericentric distances of 66 kpc, and 27 kpc, respectively. Our calculated orbital parameters are by a construction similar to orbital properties obtained by Simon et al. (2020) since we used the same the distance and line-of-sight velocity of the Grus II. Its orbit has an eccentricity of 0.44, somewhat different from the 20 RR Lyrae stars associated with the Orphan stream in our study. In addition, looking at the best-fitting model of the Orphan orbit obtained by Erkal et al. (2019, see their Fig. 3 for reference) Grus II at $\phi_1 = -66.1$ deg, if considered as the Orphan progenitor, should have largely different line-of-sight velocity than it was measured by Hansen et al. (2020), but further examination is highly desirable.

Some orbital properties of likely Orphan stream members are examined in the $E - L_{\rm z}$ plane and are displayed in Fig. 6. All of Orphan RR Lyrae stars clusters on positive values of $L_{\rm z}$ denoting its prograde orbit (thus confirming previous findings by, e.g., Newberg et al. 2010), and high-energy region. Grus II falls right in the middle of our distribution of RR Lyrae stars, partially supporting the hypothesis of Grus II being the progenitor of the Orphan stellar stream. Unfortunately, large uncertainties in actions and energies prohibit a sensible comparison in the multivariate parameter space between Orphan RR Lyrae stars and Grus II. At the current error budget, multivariate analysis in the action space would lead to a large number of false-positive candidates for membership with Grus II.

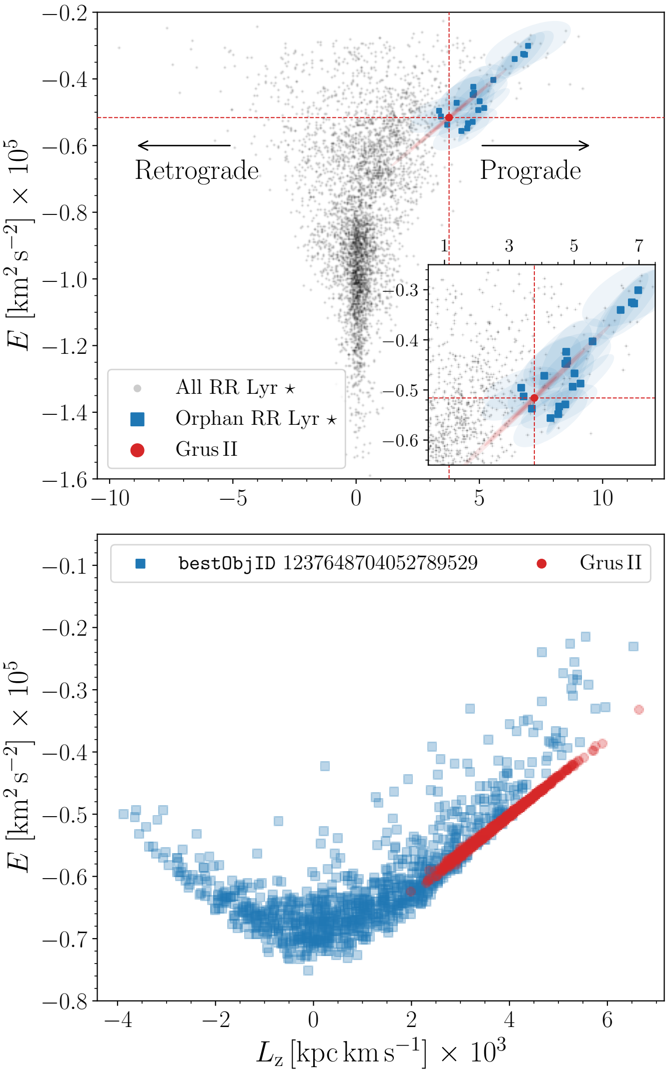

Fig. 6. Distribution of the orbital energy E vs. the z-component of the angular momentum $L_{\rm z}$ (*top panel*). The *bottom panel* shows an example of the multivariate non-normal distribution of energies E vs. angular momenta for one of the stars from our sample (represented with blue squares) and Grus II (denoted with red circles). The underlying gray points in the *upper panel* represent the entire RR Lyrae sample fulfilling the condition in Eq. (1). The blue squares represent the RR Lyrae variables associated with the Orphan stellar stream. Each point is accompanied with an error ellipse estimated based on our Monte Carlo simulation. The position of Grus II is marked with the red dot and dashed lines accompanied by error ellipses representing the covariances.

5.2.2. An elusive chemical connection between the Orphan stream and Grus II

The broad [Fe/H] distribution of the Orphan stream supports its likely origin from a dwarf-like galaxy as was pointed out by several previous studies (e.g., Sesar et al. 2013; Casey et al. 2013, 2014; Koposov et al. 2019; Fardal et al. 2019). The work by Casey et al. (2013, 2014) used low- and high-resolution spectra of K-giants to study the chemical and kinematical properties of the Orphan stream. Using *Gaia* proper motions, we were able

---

[16] For details on the disk potential see Bovy (2015).

to clean the K-giants sample from the obvious outliers using our method described in Sect. 3 and the K19 RR Lyrae sample as a reference. We note that we did not use the radial velocities determined in our study, since they do not cover the coordinate region examined by Casey et al. (2013, 2014), thus our membership probabilities are only based on coordinates and proper motions.

We found that from both studies (Casey et al. 2013, 2014) only two stars[17] can be considered as likely members (having set the $p(A|B) > 0.05$ threshold). Similarly to the proper motion membership provided by Fardal et al. (2019), we associate star OSS-8 with the Orphan stream. Unlike Fardal et al. (2019) we do not associate OSS-6 and OSS-14 with the stream given their low $p(A|B) = 0.02$ and $p(A|B) = 0.0$, respectively. This does neither significantly affect the observed metallicity spread, nor the assumed peak in its distribution. The two stars associated with the Orphan stream in our analysis exhibit very different metallicities namely; −2.82, −1.62 dex (based on tab. 1 in Casey et al. 2013) covering the entire metallicity domain described in Sesar et al. (2013) or covered by our sample of nonvariable stars (see Sect. 4.2 and Fig. 5 for details).

The spectroscopic study by Hansen et al. (2020) provides a detailed abundance analysis for three likely Grus II members located on the RGB. The low number of stars with extensive abundance patterns associated both with the Orphan stellar stream and the Grus II dwarf galaxy prohibits any detailed chemical tagging. Nevertheless, the iron abundance $[\mathrm{Fe/H}] = (-2.49; -2.69; -2.94)$ dex for three red giants linked with Grus II permits a tentative discussion about their possible connection with the Orphan stream on the basis of its metallicity distribution. The metallicities of the three Grus II giants fall onto the metal-poor end of Orphan's metallicity distribution as traced by several independent sources: K-giants, RR Lyrae stars (Casey et al. 2013; Sesar et al. 2013), and our RR Lyrae and nonvariable stellar sample.

In general, the UFDs are almost exclusively old and metal-poor. On the other hand, considering a rather massive dwarf galaxy, it is expected to undergo a few episodes of star formation. This will result in stars with higher metallicities being centrally concentrated (due to past and/or ongoing star formation), while the more metal-poor stars are distributed all over the galaxy (Harbeck et al. 2001; Grebel et al. 2003; Crnojević et al. 2010; Lianou et al. 2010; Hendricks et al. 2014). Thus, when a given dwarf enters a parent galaxy potential, it is subdued by the strong gravitational forces, which inevitably results in a tidal disruption of its peripherals, and later the dwarf itself. The outlined paradigm leads to the formation of a metallicity gradient, where metal-poor stars are stripped first followed by the metal-rich core. Such a metallicity gradient has been reported, for example, in the Sagittarius dwarf and stream (see, e.g., Bellazzini et al. 1999; McDonald et al. 2013; Hayes et al. 2020). We note that dwarf galaxies with inverse metallicity gradients have been observed in other galaxy systems and at higher redshifts (e.g., Wang et al. 2019; Grossi et al. 2020) but so far not in the Local Group.

Concerning the presumed metallicity distribution between the stream and its progenitor, we assessed the probability of observing three metal-poor red giants with respect to the metallicity distribution of the Orphan stream. We employed the Gaussian kernel density estimate (KDE) from the `scikit-learn` library (Pedregosa et al. 2011) to describe the aforementioned metallicity distribution. Using the `GridSearchCV` module from the `scikit-learn` library, with 10-fold cross-validation, we selected the most suitable bandwidth (0.176) of the Gaussian kernel for the metallicity distribution of the RGB stars associated with the Orphan stream. The resulting KDE is displayed in Fig. 5. Using the estimated metallicity KDE, we randomly drew three values simulating the random pick in observing three red giants in Grus II. We searched for instances where we would pick three stars with $[\mathrm{Fe/H}] < -2.4$ dex. Based on one million evaluations, such an event happened only in approximately 0.2 percent of the cases. We note that a similar results holds even when we assume $[\mathrm{Fe/H}] = -2.51 \pm 0.11$ dex from Simon et al. (2020) based on metallicities estimated from the Calcium triplet. Thus, connecting the Grus II with the Orphan stream is rather unlikely. Taking into consideration the discrepancy between metallicities in high-resolution studies and SDSS stellar parameters (Smolinski et al. 2011), we would expect this probability to go even lower.

6. Summary

In this study, we presented our sample of 4247 halo RR Lyrae stars with an available 7D chemo-dynamical distribution based on the SDSS survey, mapping mainly the northern hemisphere from four out to 100 kpc. We employed our dataset to study the Orphan stellar stream with which we found 20 single mode RR Lyrae stars spatially and kinematically associated. We provide the full spatial and kinematical distribution for the identified stream members together with their spectroscopic metallicities. The average metallicity of our Orphan RR Lyrae members centers at −1.80(6) dex, thus yielding a higher metallicity than previously reported for RR Lyrae variables linked to the Orphan stream (e.g., Sesar et al. 2013). A higher average metallicity and the extended metallicity distribution could potentially shift the predicted mass of the Orphan progenitor from 10^6 to $10^7\ M_\odot$ (using the mass-metallicity relation from Kirby et al. 2013). Unfortunately, large uncertainties in systemic velocities of our RR Lyrae sample prevent us from exploring the progenitor mass for the Orphan stellar stream by means of its velocity dispersion.

Using the newly identified stream members and their line-of-sight velocities, we searched for additional nonvariable members using the spectral catalog of the SDSS survey processed by the SSPP pipeline. We found additional 54 nonvariable stars that are mainly RGB and BHB stars exhibiting different metallicity distributions -2.13 ± 0.05 dex, and -1.87 ± 0.14 dex, with dispersions of 0.23 and 0.43 dex, respectively.

The 7D chemo-dynamical distribution of the associated RR Lyrae and nonvariable stars permitted us to carry out comparison between likely Orphan stream members and a possible Orphan progenitor, Grus II, a UFD discovered in the DES (Drlica-Wagner et al. 2015; Abbott et al. 2018). Kinematically, RR Lyrae members and Grus II match in action and energy space, albeit with large uncertainties in the aforementioned parameters. The orbital properties also fit, both Orphan stream stars and Grus II follow a prograde orbit with mildly different eccentricities (0.4−0.7), and similar pericentric and apocentric passages. Since in the interaction model between the MW, the Large Magellanic Cloud, and the Orphan stream (Erkal et al. 2019), the line-of-sight velocity of Grus II does not exactly match, further investigation is called for. From the chemical perspective, using [Fe/H] from a study of three RGB stars by Hansen et al. (2020), Grus II presumably lies on the metal-poor end of the metallicity distribution of the Orphan stream. Furthermore, considering Grus II as the progenitor of the Orphan

---

[17] Marked as OSS-7 and OSS-8 in Casey et al. (2013, 2014).

stream would result in an inverse metallicity gradient between the stream and Grus II which would be unexpected, although we note that such dwarf galaxies (stellar masses below $10^{9.5}$ $M_\odot$, Grossi et al. 2020) have been observed outside the Local Group. Dwarf galaxies with an inverted metallicity gradient have been found in, for example, the Virgo cluster (Grossi et al. 2020) or at high redshifts (Cresci et al. 2010; Queyrel et al. 2012; Wang et al. 2019). Thus, linking Grus II with the Orphan stream on metallicity alone is dubious. For the reasons above we conclude that the link between Grus II and the northern part of the Orphan stream is rather unlikely.

This conclusion leaves us with two possible options to contemplate about the Orphan's stream's progenitor. One suggests that it has been already dissolved during its passage through the MW halo while the second option points toward the progenitor currently being located in the Galactic plane where high extinction severely hampers the efforts in search for MW satellites. Using our Gaussian process regressor between the equatorial coordinate α and the heliocentric distance, we looked at the expected orbit of the Orphan stream. It passes behind the Galactic plane around $d = (18 \pm 3)$ kpc which places the stream right on the edge of the assumed MW disk. Although the currently assumed mass of the Orphan progenitor (from 10^6 to 10^7 $M_\odot$) is not enought to warp the MW disk (Burke 1957; Westerhout 1957), the model passes through the strong negative vertical displacement traced by the Classical Cepheids in the outer disk (see the left-hand panel of Fig. 7 in Skowron et al. 2019).

Acknowledgements. Z. P., A. J. K. H., B. L., E. K. G., and H. L. acknowledge support by the Deutsche Forschungsgemeinschaft (DFG, German Research Foundation) – Project-ID 138713538 – SFB 881 ("The Milky Way System", subprojects A03, A05, A11). V. F. B., M. F., G. A., S. M. and P. M. M. acknowledge the financial support of the Istituto Nazionale di Astrofisica (INAF), Osservatorio Astronomico di Roma and Agenzia Spaziale Italiana (ASI) under contract to INAF: ASI 2014-049-R.0 dedicated to SSDC. G. F. has been supported by the Futuro in Ricerca 2013 (Grant RBFR13J716). Funding for the Sloan Digital Sky Survey IV has been provided by the Alfred P. Sloan Foundation, the U.S. Department of Energy Office of Science, and the Participating Institutions. MM and JPM are supported by the US National Science Foundation under Grant No. AST-1714534. We thank Marina Rejkuba for the useful discussion and thoughtful comments that helped improve the manuscript. SDSS-IV acknowledges support and resources from the Center for High Performance Computing at the University of Utah. The SDSS website is `www.sdss.org`. SDSS-IV is managed by the Astrophysical Research Consortium for the Participating Institutions of the SDSS Collaboration including the Brazilian Participation Group, the Carnegie Institution for Science, Carnegie Mellon University, Center for Astrophysics | Harvard & Smithsonian, the Chilean Participation Group, the French Participation Group, Instituto de Astrofísica de Canarias, The Johns Hopkins University, Kavli Institute for the Physics and Mathematics of the Universe (IPMU)/University of Tokyo, the Korean Participation Group, Lawrence Berkeley National Laboratory, Leibniz Institut für Astrophysik Potsdam (AIP), Max-Planck-Institut für Astronomie (MPIA Heidelberg), Max-Planck-Institut für Astrophysik (MPA Garching), Max-Planck-Institut für Extraterrestrische Physik (MPE), National Astronomical Observatories of China, New Mexico State University, New York University, University of Notre Dame, Observatário Nacional/MCTI, The Ohio State University, Pennsylvania State University, Shanghai Astronomical Observatory, United Kingdom Participation Group, Universidad Nacional Autónoma de México, University of Arizona, University of Colorado Boulder, University of Oxford, University of Portsmouth, University of Utah, University of Virginia, University of Washington, University of Wisconsin, Vanderbilt University, and Yale University. This work has made use of data from the European Space Agency (ESA) mission *Gaia* (`https://www.cosmos.esa.int/gaia`), processed by the *Gaia* Data Processing and Analysis Consortium (DPAC, `https://www.cosmos.esa.int/web/gaia/dpac/consortium`). Funding for the DPAC has been provided by national institutions, in particular the institutions participating in the *Gaia* Multilateral Agreement. The CSS survey is funded by the National Aeronautics and Space Administration under Grant No. NNG05GF22G issued through the Science Mission Directorate Near-Earth Objects Observations Program. The CRTS survey is supported by the US National Science Foundation under grants AST-0909182 and AST-1313422. This research made use of the following Python packages: `Astropy` (Astropy Collaboration 2013, 2018), `dustmaps` (Green 2018), `emcee` (Foreman-Mackey et al. 2013), `galpy` (Bovy 2015), `IPython` (Pérez & Granger 2007), `Matplotlib` (Hunter 2007), `NumPy` (Harris et al. 2020), `scikit-learn` (Pedregosa et al. 2011), and `SciPy` (Virtanen et al. 2020).

References

Abbas, M. A., Grebel, E. K., Martin, N. F., et al. 2014, MNRAS, 441, 1230
Abbott, T. M. C., Abdalla, F. B., Allam, S., et al. 2018, ApJS, 239, 18
Aguado, D. S., Ahumada, R., Almeida, A., et al. 2019, ApJS, 240, 23
Allende Prieto, C., Sivarani, T., Beers, T. C., et al. 2008, AJ, 136, 2070
Amorisco, N. C., Gómez, F. A., Vegetti, S., & White, S. D. M. 2016, MNRAS, 463, L17
Anderson, R. I., Eyer, L., & Mowlavi, N. 2013, MNRAS, 434, 2238
Asplund, M., Grevesse, N., Sauval, A. J., & Scott, P. 2009, ARA&A, 47, 481
Astropy Collaboration (Robitaille, T. P., et al.) 2013, A&A, 558, A33
Astropy Collaboration (Price-Whelan, A. M., et al.) 2018, AJ, 156, 123
Baumgardt, H., Hilker, M., Sollima, A., & Bellini, A. 2019, MNRAS, 482, 5138
Bayes, M., & Price, M. 1763, Phil. Trans. R. Soc. London, Ser. I, 53, 370
Bell, E. F., Zucker, D. B., Belokurov, V., et al. 2008, ApJ, 680, 295
Bellazzini, M., Ferraro, F. R., & Buonanno, R. 1999, MNRAS, 304, 633
Belokurov, V., Zucker, D. B., Evans, N. W., et al. 2006, ApJ, 642, L137
Belokurov, V., Evans, N. W., Irwin, M. J., et al. 2007, ApJ, 658, 337
Belokurov, V., Erkal, D., Evans, N. W., Koposov, S. E., & Deason, A. J. 2018, MNRAS, 478, 611
Bennett, M., & Bovy, J. 2019, MNRAS, 482, 1417
Binney, J. 2012, MNRAS, 426, 1324
Blanco-Cuaresma, S. 2019, MNRAS, 486, 2075
Blanco-Cuaresma, S., Soubiran, C., Heiter, U., & Jofré, P. 2014, A&A, 569, A111
Bode, P., Ostriker, J. P., & Turok, N. 2001, ApJ, 556, 93
Bonaca, A., Hogg, D. W., Price-Whelan, A. M., & Conroy, C. 2019, ApJ, 880, 38
Bovy, J. 2015, ApJS, 216, 29
Bovy, J., & Rix, H.-W. 2013, ApJ, 779, 115
Braga, V. F., Stetson, P. B., Bono, G., et al. 2016, AJ, 152, 170
Bullock, J. S., & Boylan-Kolchin, M. 2017, ARA&A, 55, 343
Burke, B. F. 1957, AJ, 62, 90
Carlberg, R. G. 2012, ApJ, 748, 20
Carretta, E., Bragaglia, A., Gratton, R., D'Orazi, V., & Lucatello, S. 2009, A&A, 508, 695
Casagrande, L., & VandenBerg, D. A. 2018, MNRAS, 479, L102
Casey, A. R., Da Costa, G., Keller, S. C., & Maunder, E. 2013, ApJ, 764, 39
Casey, A. R., Keller, S. C., Da Costa, G., Frebel, A., & Maunder, E. 2014, ApJ, 784, 19
Castelli, F., & Kurucz, R. 2003, Proc. IAU Symp. 210, poster A20
Catelan, M. 2009, Ap&SS, 320, 261
Catelan, M., Pritzl, B. J., & Smith, H. A. 2004, ApJS, 154, 633
Chadid, M., Sneden, C., & Preston, G. W. 2017, ApJ, 835, 187
Chambers, K. C., Magnier, E. A., Metcalfe, N., et al. 2016, ArXiv e-prints [arXiv:1612.05560]
Choi, J., Dotter, A., Conroy, C., et al. 2016, ApJ, 823, 102
Ciddor, P. E. 1996, Appl. Opt., 35, 1566
Clementini, G., Ripepi, V., Molinaro, R., et al. 2019, A&A, 622, A60
Coppola, G., Marconi, M., Stetson, P. B., et al. 2015, ApJ, 814, 71
Cresci, G., Mannucci, F., Maiolino, R., et al. 2010, Nature, 467, 811
Crestani, J., Fabrizio, M., Braga, V. F., et al. 2021, ApJ, 908, 20
Crnojević, D., Grebel, E. K., & Koch, A. 2010, A&A, 516, A85
Dawson, K. S., Schlegel, D. J., Ahn, C. P., et al. 2013, AJ, 145, 10
de Boer, T. J. L., Erkal, D., & Gieles, M. 2020, MNRAS, 494, 5315
Dekel, A., & Silk, J. 1986, ApJ, 303, 39
Di Criscienzo, M., Marconi, M., & Caputo, F. 2004, ApJ, 612, 1092
Dotter, A. 2016, ApJS, 222, 8
Drake, A. J., Djorgovski, S. G., Mahabal, A., et al. 2009, ApJ, 696, 870
Drake, A. J., Catelan, M., Djorgovski, S. G., et al. 2013a, ApJ, 763, 32
Drake, A. J., Catelan, M., Djorgovski, S. G., et al. 2013b, ApJ, 765, 154
Drake, A. J., Graham, M. J., Djorgovski, S. G., et al. 2014, ApJS, 213, 9
Drlica-Wagner, A., Bechtol, K., Rykoff, E. S., et al. 2015, ApJ, 813, 109
Eisenstein, D. J., Weinberg, D. H., Agol, E., et al. 2011, AJ, 142, 72
Erkal, D., & Belokurov, V. 2015, MNRAS, 450, 1136
Erkal, D., Belokurov, V., Laporte, C. F. P., et al. 2019, MNRAS, 487, 2685
Fabrizio, M., Bono, G., Braga, V. F., et al. 2019, ApJ, 882, 169
Fardal, M. A., van der Marel, R. P., Sohn, S. T., & del Pino Molina, A. 2019, MNRAS, 486, 936
Fellhauer, M., Evans, N. W., Belokurov, V., et al. 2007, MNRAS, 375, 1171

Fiorentino, G., Bono, G., Monelli, M., et al. 2015, ApJ, 798, L12
For, B.-Q., Sneden, C., & Preston, G. W. 2011, ApJS, 197, 29
Foreman-Mackey, D., Hogg, D. W., Lang, D., & Goodman, J. 2013, PASP, 125, 306
Gaia Collaboration (Brown, A. G. A., et al.) 2021, A&A, in press, `https://doi.org/10.1051/0004-6361/202039657`
Geller, A. M., Latham, D. W., & Mathieu, R. D. 2015, AJ, 150, 97
Gilmore, G., Wilkinson, M. I., Wyse, R. F. G., et al. 2007, ApJ, 663, 948
Gravity Collaboration (Abuter, R., et al.) 2019, A&A, 625, L10
Grebel, E. K., Gallagher, J. S. I., & Harbeck, D. 2003, AJ, 125, 1926
Green, G. 2018, J Open Sour. Software, 3, 695
Grillmair, C. J. 2006, ApJ, 645, L37
Grillmair, C. J., & Dionatos, O. 2006, ApJ, 643, L17
Grossi, M., García-Benito, R., Cortesi, A., et al. 2020, MNRAS, 498, 1939
Hajdu, G., Dékány, I., Catelan, M., Grebel, E. K., & Jurcsik, J. 2018, ApJ, 857, 55
Hanke, M., Hansen, C. J., Koch, A., & Grebel, E. K. 2018, A&A, 619, A134
Hanke, M., Koch, A., Prudil, Z., Grebel, E. K., & Bastian, U. 2020, A&A, 637, A98
Hansen, T. T., Marshall, J. L., Simon, J. D., et al. 2020, ApJ, 897, 183
Harbeck, D., Grebel, E. K., Holtzman, J., et al. 2001, AJ, 122, 3092
Harris, C. R., Millman, K. J., van der Walt, S. J., et al. 2020, Nature, 585, 357
Hayes, C. R., Majewski, S. R., Hasselquist, S., et al. 2020, ApJ, 889, 63
Helmi, A. 2020, ARA&A, 58, 205
Helmi, A., White, S. D. M., de Zeeuw, P. T., & Zhao, H. 1999, Nature, 402, 53
Helmi, A., Babusiaux, C., Koppelman, H. H., et al. 2018, Nature, 563, 85
Hendel, D., Scowcroft, V., Johnston, K. V., et al. 2018, MNRAS, 479, 570
Hendricks, B., Koch, A., Walker, M., et al. 2014, A&A, 572, A82
Hernquist, L. 1990, ApJ, 356, 359
Hu, W., Barkana, R., & Gruzinov, A. 2000, Phys. Rev. Lett., 85, 1158
Hunter, J. D. 2007, Comput. Sci. Eng., 9, 90
Ibata, R., Lewis, G. F., Irwin, M., Totten, E., & Quinn, T. 2001, ApJ, 551, 294
Ibata, R. A., Lewis, G. F., Irwin, M. J., & Quinn, T. 2002, MNRAS, 332, 915
Ibata, R. A., Malhan, K., & Martin, N. F. 2019, ApJ, 872, 152
Ibata, R., Thomas, G., Famaey, B., et al. 2020, ApJ, 891, 161
Iben, I. J., & Huchra, J. 1971, A&A, 14, 293
Johnston, K. V., Zhao, H., Spergel, D. N., & Hernquist, L. 1999, ApJ, 512, L109
Johnston, K. V., Law, D. R., & Majewski, S. R. 2005, ApJ, 619, 800
Jurcsik, J., & Kovacs, G. 1996, A&A, 312, 111
Jurcsik, J., Clement, C., Geyer, E. H., & Domsa, I. 2001, AJ, 121, 951
Jurcsik, J., Hajdu, G., Dékány, I., et al. 2018, MNRAS, 475, 4208
Kaiser, N., Burgett, W., Chambers, K., et al. 2010, in Ground-based and Airborne Telescopes III, SPIE Conf. Ser., 7733, 77330E
Kauffmann, G., White, S. D. M., & Guiderdoni, B. 1993, MNRAS, 264, 201
Kendall, M. G. 1938, Biometrika, 30, 81
Kim, M. G. 2000, Commun. Stat. - Theory. Methods, 29, 1511
Kim, D.-W., & Bailer-Jones, C. A. L. 2016, A&A, 587, A18
Kirby, E. N., Cohen, J. G., Guhathakurta, P., et al. 2013, ApJ, 779, 102
Koch, A. 2009, Astron. Nachr., 330, 675
Koposov, S. E., Rix, H.-W., & Hogg, D. W. 2010, ApJ, 712, 260
Koposov, S. E., Belokurov, V., Li, T. S., et al. 2019, MNRAS, 485, 4726
Küpper, A. H. W., Balbinot, E., Bonaca, A., et al. 2015, ApJ, 803, 80
Landolt, A. U. 2009, AJ, 137, 4186
Landolt, A. U., & Uomoto, A. K. 2007, AJ, 133, 768
Law, D. R., & Majewski, S. R. 2010, ApJ, 714, 229
Layden, A. C. 1994, AJ, 108, 1016
Lee, Y. S., Beers, T. C., Sivarani, T., et al. 2008a, AJ, 136, 2022
Lee, Y. S., Beers, T. C., Sivarani, T., et al. 2008b, AJ, 136, 2050
Lenz, P., & Breger, M. 2004, in The A-Star Puzzle, eds. J. Zverko, J. Ziznovsky, S. J. Adelman, & W. W. Weiss, IAU Symp., 224, 786
Lianou, S., Grebel, E. K., & Koch, A. 2010, A&A, 521, A43
Lindegren, L., Klioner, S. A., Hernández, J., et al. 2021, A&A, in press, `https://doi.org/10.1051/0004-6361/202039709`
Liu, T. 1991, PASP, 103, 205
Mahalanobis, P. C. 1936, Proc. Nat. Inst. Sci. (Calcutta), 2, 49
Malhan, K., & Ibata, R. A. 2018, MNRAS, 477, 4063
Marconi, M., Coppola, G., Bono, G., et al. 2015, ApJ, 808, 50
Marconi, M., Bono, G., Pietrinferni, A., et al. 2018, ApJ, 864, L13
Martínez-Vázquez, C. E., Vivas, A. K., Gurevich, M., et al. 2019, MNRAS, 490, 2183
Mateu, C., Read, J. I., & Kawata, D. 2018, MNRAS, 474, 4112
McConnachie, A. W. 2012, AJ, 144, 4
McConnachie, A. W., & Venn, K. A. 2020, Res. Notes AAS, 4, 229
McDonald, I., Zijlstra, A. A., Sloan, G. C., et al. 2013, MNRAS, 436, 413
Miyamoto, M., & Nagai, R. 1975, PASJ, 27, 533
Molnár, L., Plachy, E., Juhász, Á. L., & Rimoldini, L. 2018, A&A, 620, A127
Muraveva, T., Delgado, H. E., Clementini, G., Sarro, L. M., & Garofalo, A. 2018, MNRAS, 481, 1195
Navarro, J. F., Frenk, C. S., & White, S. D. M. 1997, ApJ, 490, 493
Neeley, J. R., Marengo, M., Bono, G., et al. 2017, ApJ, 841, 84
Neeley, J. R., Marengo, M., Freedman, W. L., et al. 2019, MNRAS, 490, 4254
Newberg, H. J., & Carlin, J. L. 2016, in Tidal Streams in the Local Group and Beyond, (Springer International Publishing), Astrophys. Space Sci. Lib., 420
Newberg, H. J., Yanny, B., Rockosi, C., et al. 2002, ApJ, 569, 245
Newberg, H. J., Willett, B. A., Yanny, B., & Xu, Y. 2010, ApJ, 711, 32
Pancino, E., Britavskiy, N., Romano, D., et al. 2015, MNRAS, 447, 2404
Paxton, B., Bildsten, L., Dotter, A., et al. 2011, ApJS, 192, 3
Paxton, B., Cantiello, M., Arras, P., et al. 2013, ApJS, 208, 4
Paxton, B., Marchant, P., Schwab, J., et al. 2015, ApJS, 220, 15
Pedregosa, F., Varoquaux, G., Gramfort, A., et al. 2011, J. Mach. Learn. Res., 12, 2825
Pérez, F., & Granger, B. E. 2007, Comput. Sci. Eng., 9, 21
Preston, G. W., Sneden, C., Chadid, M., Thompson, I. B., & Shectman, S. A. 2019, AJ, 157, 153
Price-Whelan, A. M., Mateu, C., Iorio, G., et al. 2019, AJ, 158, 223
Prudil, Z., Smolec, R., Skarka, M., & Netzel, H. 2017, MNRAS, 465, 4074
Prudil, Z., Dékány, I., Grebel, E. K., & Kunder, A. 2020, MNRAS, 492, 3408
Queyrel, J., Contini, T., Kissler-Patig, M., et al. 2012, A&A, 539, A93
Rasmussen, C. E., & Williams, C. K. I. 2005, Gaussian Processes for Machine Learning (Adaptive Computation and Machine Learning) (The MIT Press)
Sales, L. V., Helmi, A., Starkenburg, E., et al. 2008, MNRAS, 389, 1391
Savino, A., Koch, A., Prudil, Z., Kunder, A., & Smolec, R. 2020, A&A, 641, A96
Schlafly, E. F., & Finkbeiner, D. P. 2011, ApJ, 737, 103
Schönrich, R. 2012, MNRAS, 427, 274
Schönrich, R., Binney, J., & Dehnen, W. 2010, MNRAS, 403, 1829
Sesar, B. 2012, AJ, 144, 114
Sesar, B., Ivezić, Ž., Grammer, S. H., et al. 2010, ApJ, 708, 717
Sesar, B., Grillmair, C. J., Cohen, J. G., et al. 2013, ApJ, 776, 26
Sesar, B., Hernitschek, N., Mitrović, S., et al. 2017, AJ, 153, 204
Shipp, N., Drlica-Wagner, A., Balbinot, E., et al. 2018, ApJ, 862, 114
Simon, J. D., Li, T. S., Erkal, D., et al. 2020, ApJ, 892, 137
Skowron, D. M., Skowron, J., Mróz, P., et al. 2019, Acta Astron., 69, 305
Smee, S. A., Gunn, J. E., Uomoto, A., et al. 2013, AJ, 146, 32
Smolec, R. 2005, Acta Astron., 55, 59
Smolec, R., Soszyński, I., Udalski, A., et al. 2015, MNRAS, 447, 3756
Smolinski, J. P., Lee, Y. S., Beers, T. C., et al. 2011, AJ, 141, 89
Sneden, C. A. 1973, PhD Thesis, The University of Texas at Austin, USA
Sneden, C., Preston, G. W., Chadid, M., & Adamów, M. 2017, ApJ, 848, 68
Soszyński, I., Smolec, R., Dziembowski, W. A., et al. 2016, MNRAS, 463, 1332
Soszyński, I., Udalski, A., Szymański, M. K., et al. 2017, Acta Astron., 67, 297
Springel, V., Wang, J., Vogelsberger, M., et al. 2008, MNRAS, 391, 1685
Stoughton, C., Lupton, R. H., Bernardi, M., et al. 2002, AJ, 123, 485
Szeidl, B., Hurta, Z., Jurcsik, J., Clement, C., & Lovas, M. 2011, MNRAS, 411, 1744
VandenBerg, D. A., Brogaard, K., Leaman, R., & Casagrande, L. 2013, ApJ, 775, 134
Virtanen, P., Gommers, R., Oliphant, T. E., et al. 2020, Nat. Methods, 17, 261
Wang, X., Jones, T. A., Treu, T., et al. 2019, ApJ, 882, 94
Westerhout, G. 1957, Bull. Astr. Inst. Netherlands, 13, 201
Yanny, B., Rockosi, C., Newberg, H. J., et al. 2009, AJ, 137, 4377
York, D. G., Adelman, J., Anderson, J. E., et al. 2000, AJ, 120, 1579
Zinn, R., & West, M. J. 1984, ApJS, 55, 45

Appendix A: Processing the photometric data from CSS

A.1. Processing known RR Lyrae in CSS and Gaia

Our initial step in the verification of our sample was to establish the dominant pulsation period. Thus, we retrieved the pulsation periods for stars in our sample that were identified as RR Lyrae stars both in CSS and *Gaia* EDR3 (Drake et al. 2013a,b, 2014; Abbas et al. 2014; Clementini et al. 2019), and compared their pulsation periods. When the difference between periods in *Gaia* and CSS was larger than 0.005 days, we performed a period analysis using the `Period04` software (Lenz et al. 2004) on the CSS data in order to establish the dominant period. Once the variability periods P were secured, we focused on the determination of the time of brightness maxima M_0. We proceeded iteratively: first, we phased the retrieved CSS light curves using the determined periods and as a time of brightness maxima we selected the brightest point on the light curve. In the second step we decomposed the light curves using the Fourier decomposition:

$$m\,(t) = A_0 + \sum_{i=1}^{n} A_i \cdot \cos\left(2\pi k\,(\mathrm{MJD} - M_0)\,/P + \varphi_i\right), \qquad \text{(A.1)}$$

where φ_i and A_i stand for phases and amplitudes, and MJD represents the Modified Julian Date at the time of observation, and A_0 represents the mean magnitude. The optimal degree, n, of the Fourier decomposition was estimated by gradually increasing the order until the condition on Fourier amplitude was broken $A_i/\sigma_i > 4$. From the Fourier fit, we determined the phase of the brightest point and added its period-corrected value from the initial M_0^{init} creating a new, updated M_0^{upd} which entered again in the first step (see an example in Fig. A.1). After a few iterations (usually up to 5) we derived a final time of brightness maxima. We note here that for the subsequent spectroscopic analysis (see Appendix B) we favored M_0 determined from the analysis of CSS data due to a larger number of observations (as compared to *Gaia*), and because the CSS photometric observations were conducted roughly at the same time as the SDSS observations. This ensured a consistent classification of our sample since RR Lyrae stars can rapidly change their pulsation mode within a few years (see; e.g., Soszyński et al. 2017). Furthermore, strong period changes (especialy in the first-overtone pulsators, see, i.e., Jurcsik et al. 2001; Szeidl et al. 2011) can introduce an additional source of uncertainty in the determination of M_0.

In the next step, we visually verified the variability of the individual phased light curves using the CSS photometry, and we removed stars with no signs of luminosity variation. Alongside this step, using a Fourier decomposition, we determined basic light curve parameters for the RR Lyrae sample, for example, pulsation amplitudes Amp$^{V\mathrm{css}}$[18], rise time RT$^{V\mathrm{css}}$[19], amplitude ratios (R_{21}, R_{31}) and phase differences (φ_{21}, φ_{31}) defined as follows:

$$\varphi_{i1} = \varphi_i - i\varphi_1 \;\; R_{i1} = \frac{A_i}{A_1}. \qquad \text{(A.2)}$$

The estimated photometric parameters allowed us to robustly assess the pulsation subclasses (RRab, RRc, and RRd) of the studied RR Lyrae stars. Based on their position in the period-amplitude diagram and amplitude ratio vs. pulsation period, we divided them into the two categories RRab and RRc[20]. Variables on the borderline between both classes were examined further using an automated routine that removed the dominant pulsation mode and searched for signs of an additional mode that would coincide with a period ratio typical for double-mode RR Lyrae stars ($P_{1\mathrm{O}}/P_{\mathrm{F}}$ from 0.68 to 0.76, Smolec et al. 2015; Soszyński et al. 2016; Prudil et al. 2017). In the end, variables with signs of double-mode behavior were removed from our sample.

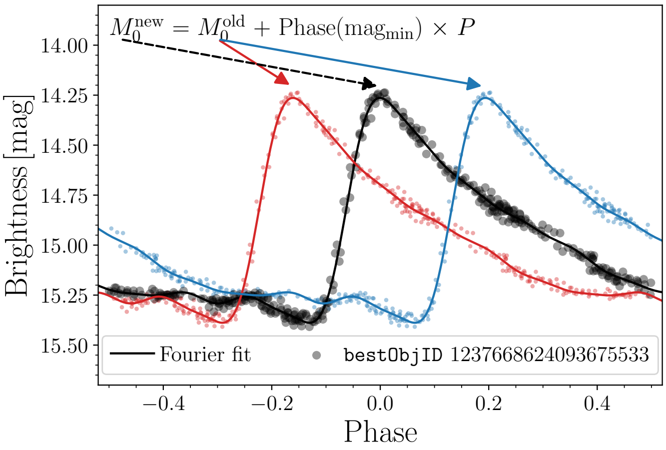

Fig. A.1. Example of the M_0 determination based on CSS photometry for one of the sample stars. The blue and red dots represent erroneous M_0 that were subsequently corrected by a phase shift of the time of brightness maxima (determined from the Fourier fit) multiplied by the pulsation period.

A.2. Searching for new RR Lyrae stars in CSS data

Taking advantage of the extensive SDSS sample and available CSS photometry, we conducted a new search for RR Lyrae stars, similar to the one performed in Hanke et al. (2020). As an initial step, we removed stars that did not have an effective temperature determined using the SSPP pipeline, assuming that they are extragalactic sources. In a second step, we looked at the color space of our confirmed RR Lyrae sample, using SDSS multiband photometry. Based on their color distribution, we applied rectangular color cuts on the entire SDSS spectral sample:

$$-1.0 < (u - g) < 1.4 \qquad \text{(A.3)}$$
$$-0.1 < (g - r) < 0.35 \qquad \text{(A.4)}$$
$$-0.1 < (r - i) < 0.15 \qquad \text{(A.5)}$$
$$-0.15 < (i - z) < 0.15. \qquad \text{(A.6)}$$

We note that our color conditions are similar to the ones used by Sesar et al. (2010) and Abbas et al. (2014), only more restricted. In addition, we did not use dereddened magnitudes.

Using the sample selected on the SDSS products, we retrieved their CSS photometry and searched for signs of variability using the `upsilon` software package[21] (Kim & Bailer-Jones 2016). This software searches for variability in the provided photometric data and yields a classification (and class probability) of the variable objects based on the shape of their light curves. To ensure

---

[18] Defined as a magnitude difference between the faintest and brightest point of the Fourier fit.

[19] Determined from the Fourier fit as a phase difference between the brightest and faintest point.

[20] We note that we identified some RRd pulsators but they were not used in our study.

[21] Accessible at: `https://github.com/dwkim78/upsilon`

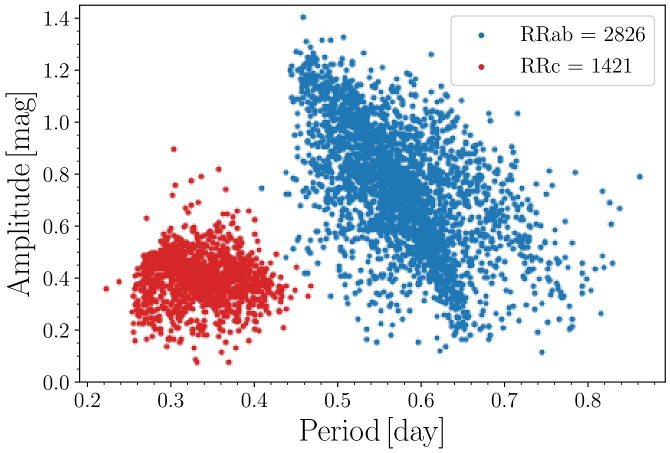

Fig. A.2. Period-amplitude diagram for the studied sample of RR Lyrae stars. Blue and red dots represent the fundamental and first overtone pulsators, respectively.

a correct classification, we selected for further examination only stars marked as RR Lyrae stars with a class probability above 50%. Then, using the determined pulsation periods from the `upsilon` package we determined M_0 (as described above), visually verified their periodicity in the phased light curves and removed the misclassified stars. For the final (pure) sample, we determined the Fourier coefficients and classified RR Lyrae in subclasses.

As a last step, we cross-matched our sample of RR Lyrae stars with the PanSTARRS-1 (PS1) survey catalog of RR Lyrae stars (Sesar et al. 2017), where their mean magnitudes were later used for the distance estimation (see Sect. 2.2). In the end, our total sample consists of 4247 RR Lyrae stars (2826 RRab and 1421 RRc) with photometric, astrometric, and spectroscopic data that entered our analysis. In Fig. A.2 we depict the distribution of the final sample in the period-amplitude diagram.

Appendix B: Processing the spectroscopic data from SDSS

Obtaining a precise systemic velocity v_{sys} for a given RR Lyrae variable is hampered by the entanglement of the measured line-of-sight velocity, v_{los}, and the motion of the atmosphere due to pulsation. The amplitude variation of the line-of-sight velocity curves depends on the atmosphere depth. Therefore, lines formed in the upper levels of the atmosphere (e.g., the Balmer lines Hα, Hβ, etc.) yield larger amplitude variation, in contrast to metallic lines from elements like Fe or Sr, which are formed lower and thereby expose smaller variations in line-of-sight velocities. The line-of-sight velocity curves measured from lines in the upper and lower layers of the atmosphere vary not only in amplitude but also in shape (see, e.g., Fig. 1 in Sesar 2012). Thus, to estimate precisely the systemic velocity of a given RR Lyrae star one needs to follow the entire pulsation cycle or utilize line-of-sight velocity templates defined for individual spectral lines (metallic lines, Hα, Hβ, Hγ, Hδ, see Liu 1991; Sesar 2012; Braga, in prep., for instance). The aforementioned templates scale with the photometric amplitudes, hence one can determine the systemic velocity using a single spectral line, the time of the observation, ephemerides, and amplitude information from photometry.

The available spectra from the SDSS are of low resolution (≈2000) with only a few prominent lines, mainly of the Balmer series (see Fig. B.1 for an example of one of our spectra) that remain detectable throughout our sample. The spectra for individual stars were obtained from the SDSS Science Archive Server[22], and consist of the co-added spectra and individual exposures in both SDSS spectral windows (blue and red). Each exposure contains a header with information about the time of the observation and data composed of vacuum wavelengths[23] in the heliocentric frame, flux-calibrated spectra (in units of $10^{-17}\,\mathrm{erg\,s^{-1}\,cm^{-2}\,\AA^{-1}}$), and their associated errors (Stoughton et al. 2002).

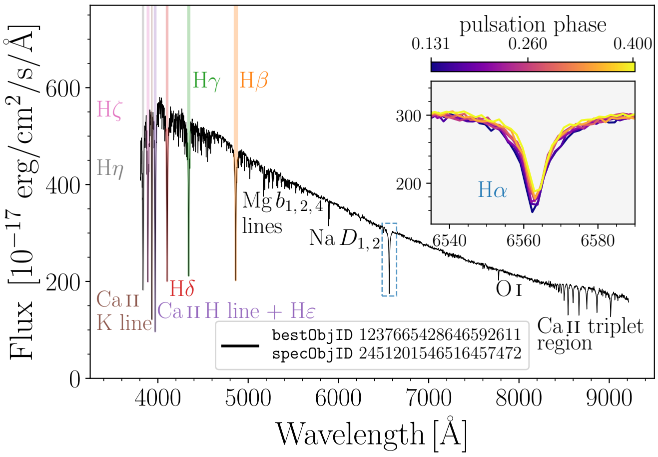

Fig. B.1. Example of an SDSS co-added spectrum (black line) for an RR Lyrae variable from our sample with the most prominent lines annotated. The individual exposures around the Hα line are depicted in the inset and color-coded based on the pulsation phase.

To consistently estimate the systemic velocities of our RR Lyrae sample, we proceeded in the following way. We separated the individual exposures (blue and red part of the spectrum) and selected four prominent Balmer lines (Hα, Hβ, Hγ, Hδ) for which we determined their line-of-sight velocities by cross-correlation with a synthetic spectrum using the `iSpec` package (Blanco-Cuaresma et al. 2014; Blanco-Cuaresma 2019). The synthesized spectra for each line were obtained through a python wrapper of the radiative transfer code MOOG (February 2017 version, Sneden 1973), using the ATLAS9 model atmospheres (Castelli & Kurucz 2003), a solar reference scale from Asplund et al. (2009), and a line list from VALD[24], all of which are implemented in `iSpec`. The synthesized spectra were calculated with respect to a set of typical stellar parameters of RR Lyrae stars (For et al. 2011; Sneden et al. 2017; Preston et al. 2019):

- $T_{\mathrm{eff}} = 6600\,\mathrm{K}$
- $\log g = 2.25\,\mathrm{dex}$
- $[\mathrm{Fe/H}] = -1.5\,\mathrm{dex}$
- Microturbulence velocity $\xi_{\mathrm{turb}} = 3.5\,\mathrm{km\,s^{-1}}$.

A region (±100 Å) around each Balmer line was cross-correlated with the synthetic spectrum. To account for the uncertainties in the flux we employed a Monte-Carlo simulation by varying the flux within its errors (assuming that they follow a Gaussian distribution). This allowed us to identify problematic spectra and to assign their v_{los} larger uncertainties than they would have using a single cross-correlation procedure.

---

[22] https://dr15.sdss.org/sas/dr15/

[23] We note that for the determination of line-of-sight velocities we converted SDSS vacuum wavelengths to the air wavelength frame using a formula from Ciddor (1996).

[24] http://vald.astro.uu.se/

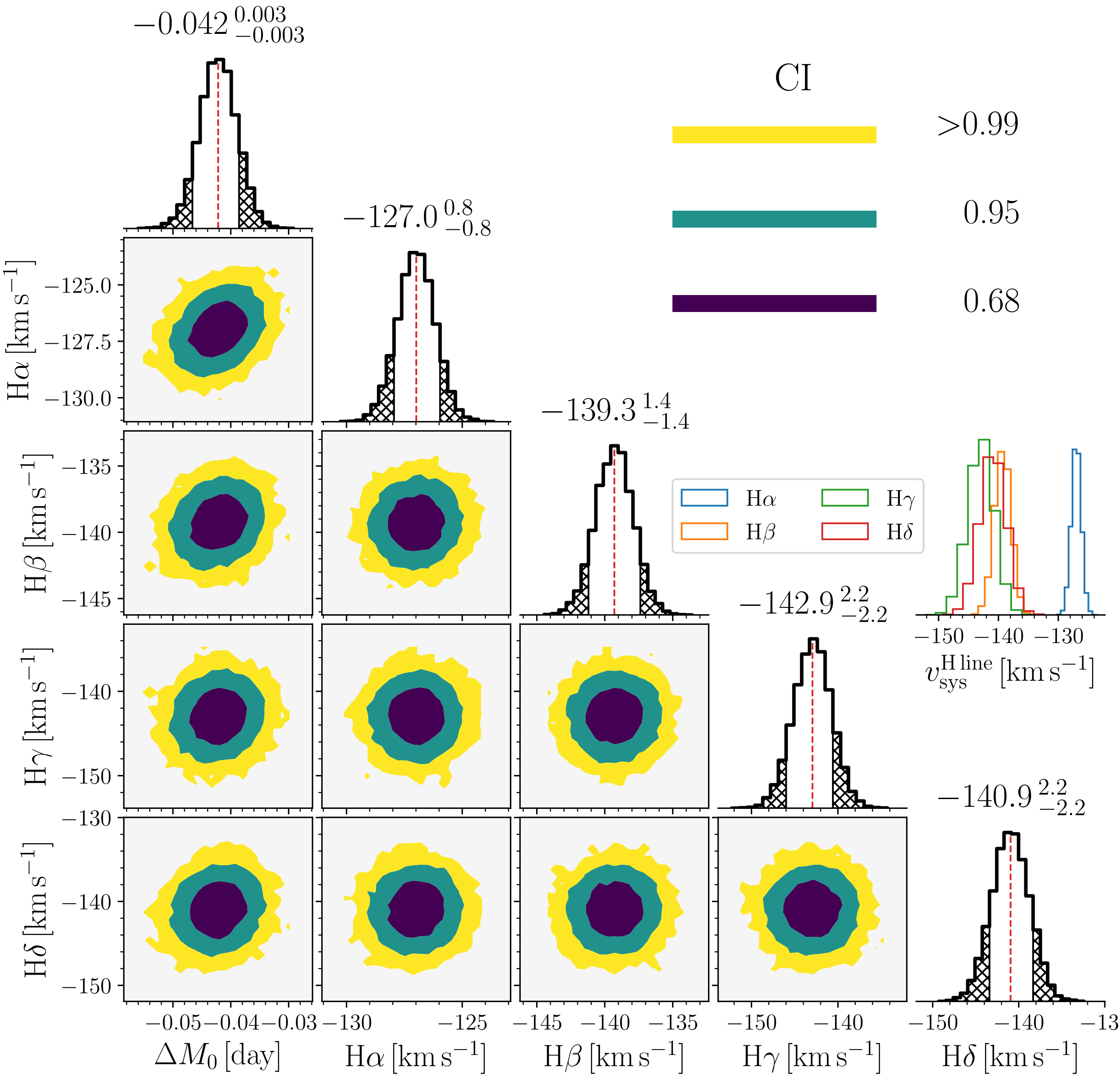

Fig. B.2. Posterior probability distribution for parameters of our model for a given RR Lyrae star in our sample (`bestObjID` = 1237649919501598744) with confidence intervals (CIs) color-coded. We see an offset between systemic velocities determined from Hβ, Hγ, and Hδ in comparison with a systemic velocity determined through the Hα line (see color histogram on the right-hand side of the figure).

Using this approach, we discarded line-of-sight velocities that failed at least one of the following conditions:

$$\left|v_{\rm los}/\sigma_{v_{\rm los}}\right| > 2 \qquad \cup \qquad \sigma_{v_{\rm los}} < 10\,{\rm km\,s^{-1}}. \tag{B.1}$$

To determine the systemic velocities of our RR Lyrae sample, we used a new set of line-of-sight velocity templates for the Balmer lines from Braga (in prep.), and scaled them by the provided linear scaling relations between the line-of-sight velocity amplitudes and the light curve amplitudes (see Braga, in prep., for details).

The systemic velocity for each Balmer line was estimated by minimizing the offset between the amplitude-scaled line-of-sight velocity templates and the measured line-of-sight velocities. For this process, we utilized the Markov chain Monte Carlo (MCMC) sampler implemented in the `emcee` package (`v.3.0.2`[25], Foreman-Mackey et al. 2013) where we maximalized the posterior probability defined in the following way:

$$p(\boldsymbol{\theta}|D) \propto p(\boldsymbol{\theta}) \times \prod^{N} p(D_n|\boldsymbol{\theta}_n), \tag{B.2}$$

where D_n represents data for an individual star in the form:

$$D_n = \left\{P_n, M_{0,n}, v_{{\rm los},n}^{\rm H\alpha}, v_{{\rm los},n}^{\rm H\beta}, v_{{\rm los},n}^{\rm H\gamma}, v_{{\rm los},n}^{\rm H\delta}\right\}, \tag{B.3}$$

and $\boldsymbol{\theta}$ the model consisting of an amplitude scaled line-of-sight velocity template for the individual Balmer line (from Braga, in

---

[25] `https://github.com/dfm/emcee/`

prep.), each shifted by the systemic velocity. In our MCMC setup we therefore sampled the following model parameters:

$$\boldsymbol{\theta}_n = \left\{\Delta M_{0,n}, v_{\mathrm{sys},n}^{\mathrm{H}\alpha}, v_{\mathrm{sys},n}^{\mathrm{H}\beta}, v_{\mathrm{sys},n}^{\mathrm{H}\gamma}, v_{\mathrm{sys},n}^{\mathrm{H}\delta}\right\}, \tag{B.4}$$

with $\Delta M_{0,n}$ representing the shift in the time of maximum light. This offset has been included since the photometric quality degrades at the faint end of our sample and the estimation of M_0 becomes challenging. This is particularly true for the first-overtone pulsators, where symmetrical light curves with lower amplitudes and larger photometric errors hamper the precise determination of M_0. The uncertainty of M_0 can affect the systemic velocity determination for stars with observations around the time of the brightness maxima, where the line-of-sight velocities change rapidly. Thus, the offset parameter, $\Delta M_{0,n}$, can compensate for such an eventuality. As a prior for our model parameters, we adopted uniform ($\mathcal{U}$) priors:

$$p(\boldsymbol{\theta}_n) = \mathcal{U}(-0.1 < \Delta M_{0,n} < 0.1) \ \cap \tag{B.5}$$

$$\mathcal{U}(\bar{v}_{\mathrm{los}}^{\mathrm{H\,line}} - 130, \bar{v}_{\mathrm{los}}^{\mathrm{H\,line}} + 130), \tag{B.6}$$

where $\bar{v}_{\mathrm{los}}^{\mathrm{H\,line}}$ represents the median velocity for all lines, with the value 130 km s^{-1} characterizing the maximal line-of-sight velocity amplitude for an RR Lyrae star with $\mathrm{Amp}^{V_{\mathrm{CSS}}} \approx 1.4$ mag. $p(D_n, \boldsymbol{\theta}_n)$ represents the likelihood for each line of a given star:

$$p(D_n, \boldsymbol{\theta}) = \mathcal{N}(v_{\mathrm{los}}^{\mathrm{H\,line}}, \sigma_{v_{\mathrm{los}}^{\mathrm{H\,line}}} | v_{\mathrm{los}}^{\mathrm{H\,model}}), \tag{B.7}$$

where $v_{\mathrm{los}}^{\mathrm{H\,model}}$ represents a velocity value for a given phase of the observation $\vartheta = (\mathrm{MJD} - M_0 + \Delta M_0)/P$, from the amplitude-scaled line-of-sight velocity template shifted by $v_{\mathrm{sys}}^{\mathrm{H\,line}}$.

To estimate the posterior distribution of our model parameters, we ran `emcee` with 48 walkers for an initial 200 steps as burn-in and then restarted the sampler for an additional 2200 steps. Figure B.2 depicts the posterior likelihood distribution of the model parameters $\boldsymbol{\theta}$ for a given RR Lyrae star from our sample.

While examining the systemic velocities determined from individual lines, we noticed a non-negligible offset in systemic velocities between individual lines, where values determined on the blue end of the spectrum showed on average smaller values than the lines on the red end. We further examined this discrepancy in nonvariable stars[26] associated with three star clusters (M 13, M 15, and M 67), where we performed a piecewise cross-correlation in the following way: for each exposure of a given star, we divided the spectrum into three sections based on wavelength;

$$\lambda_1 = (4000; 4500)\text{Å} \tag{B.8}$$

$$\lambda_2 = (4500; 5000)\text{Å} \tag{B.9}$$

$$\lambda_3 = (5500; 7000)\text{Å}. \tag{B.10}$$

These three wavelength regions approximately represent spectral regions covering Hδ and Hγ (λ_1), Hβ (λ_2), and Hα (λ_3). For each part of the spectrum, we determined the line-of-sight velocity using a synthesized template spectrum generated using the SSPP pipeline-derived quantities for T_{eff}, $\log g$, and [Fe/H]. We found that the average line-of-sight velocities from individual exposures are decreasing as we move from the red, λ_3, to the blue part, λ_1, of the spectrum. The difference between the bluest and reddest regions is on average -13 km s^{-1}. In addition, a difference between the second bluest region, λ_2, and the reddest, λ_3, region was found as well (on average -10 km s^{-1}). The comparison between the known line-of-sight velocities of the three star clusters (using literature values, Geller et al. 2015; Baumgardt et al. 2019) showed that the line-of-sight velocities determined in the red region match very well literature values, while the line-of-sight velocities from the blue regions showed the aforementioned offsets.

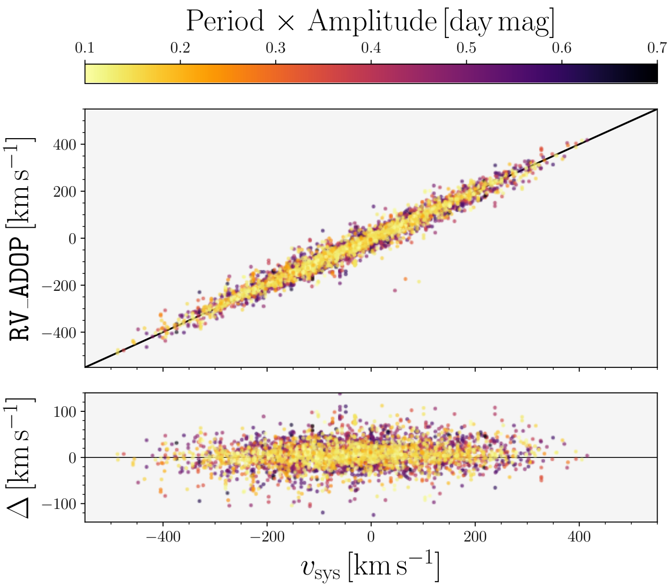

Fig. B.3. Comparison between line-of-sight velocities `RV_ADOP` derived by SSPP and our systemic velocities calculated using the line-of-sight velocity templates (*top panel*) and the residuals of their difference (*bottom panel*) with a color coding that is based on the product of pulsation period and amplitude.

We decided to include this systematic offset in the determined systemic velocities for Hγ, Hδ (shift by +13 km s^{-1}) and Hβ (shift by +10 km s^{-1}). The final systemic velocity value, v_{sys}, for a given RR Lyrae star was estimated through a weighted average using all four Balmer lines. For its uncertainty, we adopted a weighted standard deviation $\sigma_{v_{\mathrm{sys}}}$. On average, our weighted uncertainties are on the order of 14 km s^{-1}. We note here that we chose to determine the systemic velocities for each line separately instead of combining them, since this approach leads to uncertainties on the systemic velocities that are considerably lower than the precision of the SDSS wavelength calibration (<5 km s^{-1}, Lee et al. 2008b; Allende Prieto et al. 2008).

As a test for our determined systemic velocities, we compared our results (v_{sys}) with the heliocentric line-of-sight velocities, `RV_ADOP`. As expected, our systemic velocities linearly follow the values from the SSPP with a substantial scatter (≈29 km s^{-1}) which is mainly caused by the pulsations of our targets and originate from erroneous estimates on the basis of coadded spectra. In Fig. B.3, we see that stars with low amplitudes and short pulsation periods (first-overtone pulsators) exhibit a dispersion of 25 km s^{-1} and cluster around unity (black solid line in the top panel). In contrast, stars at the other end of the period-amplitude distribution exhibit a larger scatter since the chances of observing them around the time of mean line-of-sight velocity are lower. Fundamental pulsators exhibit a dispersion of 31 km s^{-1}.

---

[26] In total 162 stars covering a broad range of $\log g \approx 3$ dex, temperatures ≈4500 K, and metallicities ≈2 dex.

Appendix C: Additional figure

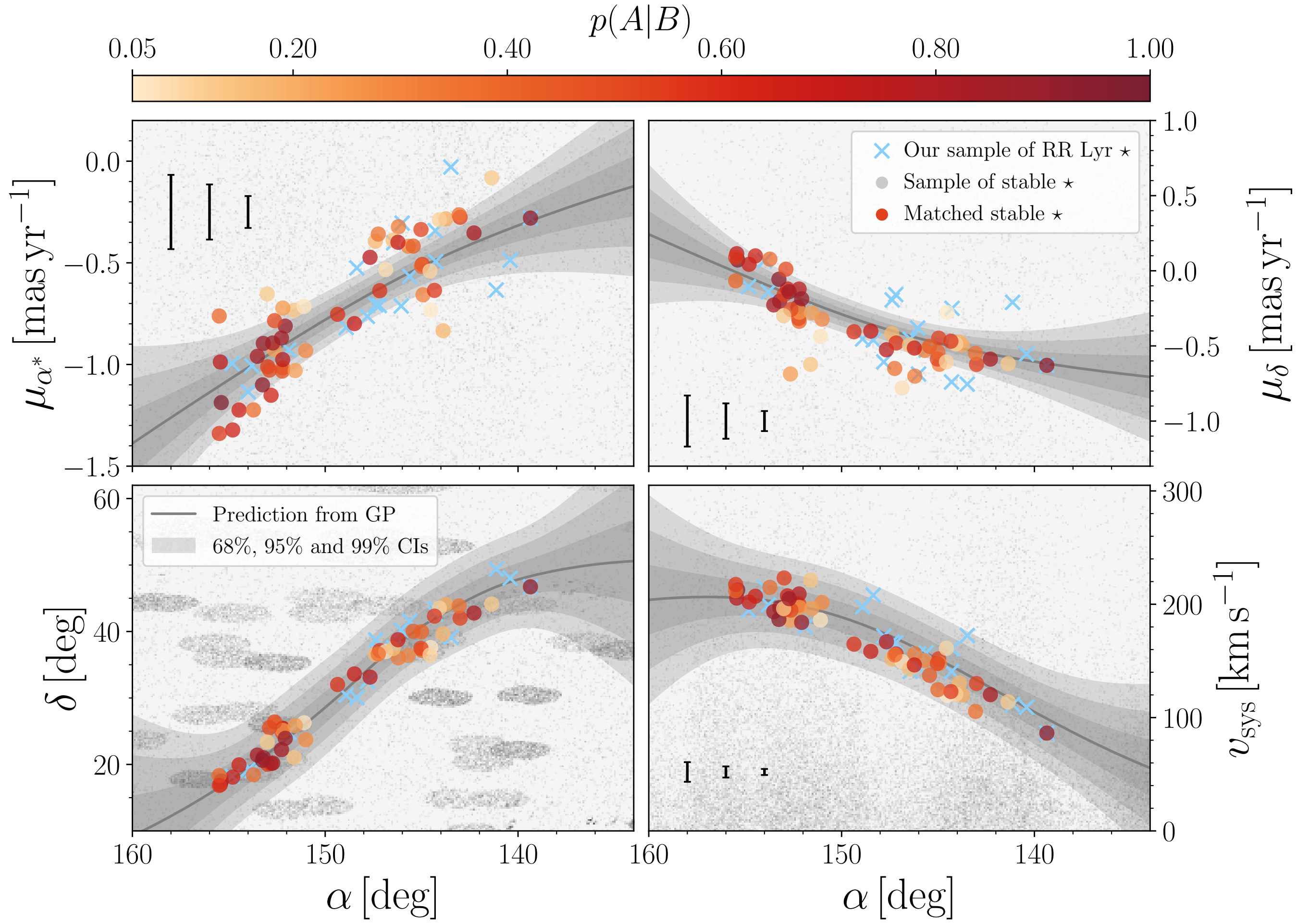

Fig. C.1. Four-parameter association of nonvariable stars with our identified sample of RR Lyrae variables (blue crosses) in the Orphan stellar stream. Similar to Fig. 3, the color coding denotes the membership probabilities $p(A|B)$ in coordinate (*bottom left panel*), proper motion (*upper panels*), and systemic velocity (*bottom right panel*) space. The gray lines and shading represent the Gaussian process regression and confidence intervals (CIs), respectively. The three error bars at the bottom of each panel denote the 15.9, 50, and 84.1 percentiles of the uncertainties on individual parameters.

Appendix D: Additional tables

Table D.1. RR Lyrae variables in our sample associated with the Orphan stream based on our analysis.

`bestObjID` (SDSS)	*Gaia* EDR3 ID	α [deg]	δ [deg]	d [kpc]	σ_d [kpc]	$v_{\rm sys}$ [km s^{-1}]	$\sigma_{v_{\rm sys}}$ [km s^{-1}]	$V_{\rm CSS}$ [mag]	$\sigma_{V_{\rm CSS}}$ [mag]	P [day]	M_0 [day]	Amp$_{V_{\rm CSS}}$ [mag]	Type	[Fe/H] [dex]	$p(A\|B)$	Note
1237660635454701712	801408324401633664	146.05782	40.22071	39.7	2.2	144.742	18.081	18.453	0.135	0.711533	54588.22739	0.57071	RRab	−1.680	0.272	K19
1237660635453718722	812926670775689984	143.48258	39.13402	42.5	2.3	172.430	15.680	18.582	0.145	0.527852	55198.25415	0.64537	RRab	−1.880	0.111	K19
1237667734496018571	625033259008713344	153.80169	19.05096	26.3	1.5	199.518	6.169	17.703	0.100	0.400190	54769.47305	0.44528	RRc	−2.030	0.915	—
1237657770706600085	1011841380940809344	140.40968	48.01452	45.4	2.5	109.058	1.139	18.922	0.158	0.367648	56402.27718	0.37343	RRc	−2.030	0.592	—
1237667782285131881	625042020741726976	153.99639	19.22272	25.8	1.4	214.922	7.709	17.667	0.098	0.645172	55563.40418	0.60377	RRab	−1.720	0.799	—
1237668290157281403	623982645584012928	154.82491	18.22602	28.0	1.6	194.632	10.047	17.870	0.108	0.578450	54628.16950	0.77584	RRab	−1.670	0.239	K19
1237657606967459944	1011263007760611456	139.35631	46.72456	42.3	2.3	86.520	12.399	18.762	0.155	0.388203	54862.20461	0.35120	RRc	−1.870	0.194	—
1237657773935624421	814812268794932608	144.29504	43.42943	41.5	2.3	140.578	6.938	18.824	0.156	0.366009	54535.33735	0.37174	RRc	−1.380	0.358	K19
1237658203425341674	813632316722202112	145.61867	41.56253	42.1	2.3	157.187	17.406	18.489	0.134	0.604208	55505.50362	0.58930	RRab	−2.190	0.188	K19
1237661851456962762	800283700102935808	147.37900	38.73692	37.6	2.1	166.666	6.772	18.135	0.117	0.286424	55212.30609	0.20096	RRc	−1.910	0.105	K19
1237664870825918615	793317812902061568	147.81260	32.49737	39.3	2.2	171.941	13.919	18.533	0.134	0.552830	54035.50252	0.65775	RRab	−1.290	0.195	—
1237665099002937435	744466232107315712	148.36049	30.02346	38.0	2.1	208.007	4.582	18.392	0.128	0.591062	53677.59556	0.40989	RRab	−2.150	0.265	K19
1237665129604317276	744807802266002432	148.91221	30.42627	34.8	1.9	197.726	35.431	18.390	0.129	0.360622	54574.20862	0.37578	RRc	−1.450	0.756	—
1237660634916913359$^{(*)}$	800895883264108416	143.91322	38.85322	43.1	2.4	53.148	12.118	18.766	0.150	0.504141	55566.42701	0.58476	RRab	−1.780	0.366	K19
1237660763234107516	799585024885253632	147.19268	37.13167	40.3	2.2	166.001	4.421	18.579	0.140	0.624428	53902.06206	0.62468	RRab	−1.870	0.068	K19
1237661850382696669	799823623206083328	146.44757	37.55324	39.9	2.2	140.716	10.239	18.329	0.130	0.624027	56313.47731	1.02146	RRab	−1.820	0.524	K19
1237661139030966463	799463292628940672	146.00854	36.26583	40.5	2.3	156.131	2.478	18.546	0.137	0.594447	54532.36231	0.76866	RRab	−1.880	0.283	K19
1237657874867421307	814635483643723520	144.27165	42.60335	43.3	2.4	160.573	12.657	18.579	0.136	0.567186	54789.53586	0.65984	RRab	−1.650	0.461	—
1237667252929036352	738597146412411904	151.89251	24.83150	31.0	1.8	180.319	22.057	17.944	0.114	0.620870	54382.54030	1.03188	RRab	−2.150	0.764	K19
1237657771780866136	1018131343366018560	141.13135	49.38273	46.9	2.7	111.560	8.632	19.028	0.161	0.342678	55119.41420	0.52122	RRc	−1.500	0.165	—

Notes. The first two columns denote the SDSS and *Gaia* EDR3 object IDs followed by their equatorial coordinates in columns three and four. Columns 5–8 list the estimated distances and systemic velocities with associated uncertainties. The parameters estimated on basis of the CSS photometry are listed in Cols. 9–13, starting with mean magnitudes, pulsation periods, time of brightness maxima, and pulsation amplitude. The following two columns list the RR Lyrae pulsation type and its conditional probability. The last columns flag stars that were associated with the Orphan stream by Koposov et al. (2019) (marked with K19) as parent population. The asterisk at `bestObjID` indicates a star that was not used as reference sample in Sect. 4.2.

Table D.2. Nonvariable stars associated with the Orphan stellar stream based on our RR Lyrae sample.

`bestObjID` (SDSS)	*Gaia* EDR3 ID	α [deg]	δ [deg]	`RV_ADOP` [km s^{-1}]	`RV_ADOP_UNC` [km s^{-1}]	g [mag]	σ_g [mag]	$T_{\rm eff}$ [K]	$\sigma_{T_{\rm eff}}$ [K]	[Fe/H] [dex]	$\sigma_{\rm [Fe/H]}$ [dex]	$\log g$ [dex]	$\sigma_{\log g}$ [dex]	$p(A\|B)$
1237667537471144142	628696866112455168	151.60904	21.04929	221.210	14.141	19.493	0.025	8311	253	−1.86	0.38	3.69	0.10	0.137
1237667211053498537	738657310314238720	152.20035	25.46991	198.841	3.985	17.955	0.019	8349	68	−1.64	0.08	3.33	0.39	0.402
1237667211590566073	738839309553409536	152.65131	26.09226	185.870	9.608	20.035	0.025	5162	216	−2.04	0.09	2.43	0.54	0.242
1237667549803446363	628835095339982976	153.21074	21.01953	197.102	2.124	17.954	0.022	5046	11	−2.03	0.08	1.92	0.17	0.893
1237667430635143257	630353112875731840	151.01106	23.71998	201.503	2.698	16.792	0.018	6107	102	−1.91	0.05	2.17	0.29	0.285
1237667736106369165	625374592944708864	152.97943	20.03164	223.173	5.468	18.203	0.017	5178	25	−2.36	0.08	2.05	0.14	0.539
1237667551413796866	629200481092312064	152.26792	22.22917	199.110	1.543	16.744	0.026	4681	105	−2.02	0.01	1.50	0.08	0.830
1237667537471930559	628871997698600704	153.51826	21.40729	193.410	3.993	18.198	0.021	5182	55	−2.27	0.06	2.01	0.07	0.824
1237667252929167431	726590372062626944	152.22576	24.81725	200.607	3.832	17.953	0.026	8139	139	−2.24	0.10	3.21	0.20	0.490
1237667253466103892	738656996781344128	152.20437	25.42895	209.124	5.578	17.728	0.019	8359	47	−1.97	0.08	3.41	0.35	0.760
1237667210516562002	738630681517008000	152.19512	25.11815	197.252	4.560	17.599	0.017	5184	50	−2.18	0.03	2.42	0.21	0.249
1237667736106303744	625388813581465856	152.80820	20.13625	207.441	8.433	18.030	0.025	8733	295	−1.90	0.08	3.09	0.50	0.645
1237660343936090311	812965188042058752	143.88747	39.66263	130.608	11.815	18.741	0.024	8381	214	−1.24	0.14	3.19	0.65	0.181
1237667430635536640	630417842327675776	152.07167	23.92788	183.996	4.831	18.144	0.018	7219	113	−1.70	0.10	3.22	0.25	0.885
1237657776082518150	817873957704595328	141.36492	44.12217	113.810	3.612	18.336	0.014	5042	44	−2.09	0.07	1.46	0.13	0.124
1237667735570088150	625510618853633152	154.46992	19.93856	207.081	5.169	18.514	0.022	5324	44	−1.94	0.16	2.40	0.09	0.658
1237661383846920453	796532505729010048	147.39971	36.55098	151.613	3.837	18.422	0.017	5039	44	−2.11	0.04	2.11	0.08	0.173
1237664667895398511$^{(*)}$	793633269661481344	147.67491	33.13807	166.882	8.848	18.772	0.026	6795	75	−1.50	0.06	2.73	0.39	0.761
1237668289083736145	3890404706979164928	155.38993	17.49104	212.624	5.389	18.767	0.027	5348	53	−2.64	0.01	2.21	0.32	0.965
1237660764307128401	799763802901092864	144.96541	37.18751	151.803	1.014	16.776	−9999	4499	409	−1.84	0.05	0.81	0.32	0.535
1237657628979953819	815043750351075328	143.73901	44.08255	119.774	5.052	18.225	0.013	5233	64	−2.32	0.03	1.67	0.43	0.206
1237657606967459944	1011263007760611456	139.35631	46.72456	86.322	9.121	19.039	0.019	6978	152	−1.92	0.04	3.27	0.64	0.922
1237657773935624352	814827352720083968	144.07772	43.51372	120.661	2.524	18.215	0.027	5009	127	−1.81	0.04	1.99	0.24	0.108
1237658205035364447	814233646503353984	143.00382	42.01405	130.019	3.959	18.514	0.015	5220	243	−1.58	0.15	1.99	0.55	0.533
1237667733959082068	624157566716484096	153.72088	18.44767	214.915	4.277	18.342	0.020	5167	22	−2.03	0.04	2.26	0.12	0.371
1237667549266509948	625435577185459968	153.25189	20.63283	186.624	11.460	19.154	0.018	8890	370	−2.01	0.12	3.57	0.19	0.928

Notes. The first two columns list the identifiers from the SDSS and *Gaia* EDR3, the following two columns the objects equatorial coordinates. Columns 5 and 6, contain the line-of-sight velocities determined by the SSPP pipeline, and the subsequent two columns provide their g-band magnitudes together with their uncertainties. Columns 9–14 list the stellar parameters derived by the SSPP pipeline. The last column represents the conditional probability for the individual star. The asterisk at `bestObjID` marks stars that are classified as RRd type stars or their classification in RR Lyrae subtypes is uncertain.

Table D.2. continued.

`bestObjID` (SDSS)	*Gaia* EDR3 ID	α [deg]	δ [deg]	`RV_ADOP` [km s^{-1}]	`RV_ADOP_UNC` [km s^{-1}]	g [mag]	σ_g [mag]	$T_{\rm eff}$ [K]	$\sigma_{T_{\rm eff}}$ [K]	[Fe/H] [dex]	$\sigma_{\rm [Fe/H]}$ [dex]	$\log g$ [dex]	$\sigma_{\log g}$ [dex]	$p(A\|B)$
1237657628979757237	815002102051985536	143.05483	43.85158	105.393	7.243	18.967	0.015	7892	106	−1.83	0.10	3.46	0.25	0.355
1237667254540173418	738864082924453888	152.62750	26.39346	194.872	4.968	19.065	0.020	5414	35	−2.33	0.05	2.60	0.14	0.501
1237667253466431572	726732209062781056	152.88857	25.52055	195.383	6.763	18.022	0.029	8132	61	−1.95	0.03	3.33	0.20	0.509
1237661384383266935	799481881247354496	145.68937	36.40120	150.277	2.854	17.956	0.018	4970	57	−2.10	0.06	1.23	0.32	0.303
1237664338242896034$^{(*)}$	745248362831928064	149.35785	32.02152	164.780	7.265	18.302	0.023	6831	120	−2.10	0.09	3.92	0.46	0.577
1237661383846461589	799409377903432192	146.20282	36.03515	156.220	9.043	18.651	0.018	8268	225	−2.68	0.14	3.03	0.11	0.322
1237657628442427527	814555842066743680	142.28329	42.77482	120.226	3.019	18.159	0.014	4819	145	−1.93	0.08	1.29	0.27	0.819
1237660764307128471	799764417079227776	144.92913	37.18107	147.710	12.770	18.565	0.014	7988	179	−1.56	0.09	3.15	0.71	0.308
1237667429562122398	630132244182398336	153.00681	23.37064	196.173	5.322	18.106	0.024	6179	158	−1.65	0.04	1.61	0.38	0.124
1237660763234107445	799585750736939136	147.17276	37.13210	156.173	1.953	17.469	0.026	4823	103	−2.38	0.06	1.71	0.09	0.580
1237661851455848669$^{(*)}$	800538438905600640	144.52811	37.58107	119.584	7.176	18.934	0.026	7130	96	−2.85	0.25	2.69	0.47	0.055
1237657874330484837	813866547058758400	144.33302	42.31582	122.986	8.127	18.775	0.018	7666	50	−2.30	0.10	3.68	0.43	0.558
1237662224591356037	794981472779226880	148.48536	33.61997	158.403	10.066	18.455	0.013	7589	103	−1.88	0.06	3.92	0.34	0.677
1237668288546865284	3890324339551568896	155.43794	16.96701	205.456	3.210	17.861	0.019	8204	31	−1.71	0.05	3.30	0.32	0.742
1237660763233976439	799560973068347520	146.86139	36.97398	149.349	6.724	18.519	0.020	8904	412	−1.10	0.53	3.49	0.46	0.078
1237660764844130395	800525317782751104	145.03387	37.48114	147.770	8.381	18.710	0.021	8643	218	−2.27	0.10	3.36	0.23	0.522
1237660343936483487	801059714792493312	145.00683	39.96981	124.638	5.739	19.099	0.022	5738	112	−1.97	0.05	2.61	0.26	0.400
1237670965928788035$^{(*)}$	623884479811567232	154.79668	18.09111	201.940	3.353	17.347	0.053	7763	122	−1.14	0.38	3.10	0.21	0.664
1237661850382696658	799820595251815552	146.47956	37.43788	142.935	3.601	18.020	0.015	4895	108	−2.45	0.05	1.27	0.16	0.156
1237667255076454406	738998051544247808	151.09596	26.26995	186.114	2.682	17.149	0.022	4924	66	−2.44	0.07	1.77	0.09	0.068
1237660763769995449	798207787789021056	144.56194	36.46507	161.170	3.906	18.441	0.020	5135	43	−2.18	0.07	1.68	0.21	0.101
1237668290157543482	623997244177536512	155.49606	18.33054	211.947	3.323	17.821	0.022	8103	18	−1.81	0.02	3.47	0.08	0.391
1237667211590172695	738914454301088896	151.55458	25.85548	196.119	2.262	17.157	0.014	4889	64	−2.06	0.05	1.59	0.12	0.241
1237670964318371898	3890296095846572160	155.49308	16.83852	217.476	1.614	17.537	0.026	5071	76	−2.00	0.04	1.79	0.11	0.555
1237660635454505093	801391389347743104	145.43703	40.03586	137.319	2.639	17.805	0.019	4909	33	−2.20	0.03	1.58	0.09	0.430
1237660962942943451	801079020669410048	146.22752	38.75768	146.472	7.459	18.594	0.017	7804	188	−1.75	0.14	3.29	0.33	0.679
1237667783895351306	625392769246309504	152.72107	20.20343	204.944	1.443	16.662	0.022	4687	156	−1.94	0.05	1.34	0.07	0.870
1237661139031425067	796535460666541696	147.24772	36.61864	155.236	5.931	18.332	0.028	6772	228	−1.25	0.16	2.46	0.57	0.353